

RESEARCH ARTICLE | APRIL 15 2021

A three-dimensional phase-field lattice Boltzmann method for incompressible two-components flows

Special Collection: [Special Issue on the Lattice Boltzmann Method](#)

Alessandro De Rosis  ; Enatri Enan 

 Check for updates

Physics of Fluids 33, 04315 (2021)

<https://doi.org/10.1063/5.0046875>



View
Online



Export
Citation

Articles You May Be Interested In

Two-relaxation time lattice Boltzmann models for the ion transport equation in electrohydrodynamic flow: D2Q5 vs D2Q9 and D3Q7 vs D3Q27

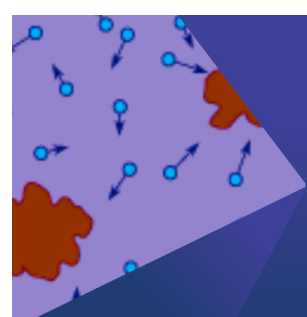
Physics of Fluids (April 2021)

Comparing classical electrodynamic theories predicting deformation of a water droplet in a tightly focused Gaussian beam

Physics of Fluids (April 2023)

Study on boiling heat transfer in a shear flow through the lattice Boltzmann method

Physics of Fluids (April 2021)



Physics of Fluids

Special Topic:

250 Years of Brownian Motion

Guest Editors: Alan Jeffrey Giacomin and Nhan Phan-Thien

[Submit Today!](#)

 AIP
Publishing

A three-dimensional phase-field lattice Boltzmann method for incompressible two-components flows

Cite as: Phys. Fluids 33, 043315 (2021); doi: 10.1063/5.0046875

Submitted: 8 February 2021 · Accepted: 13 March 2021 ·

Published Online: 15 April 2021



View Online



Export Citation



CrossMark

Alessandro De Rosis^{a)} and Enatri Enan

AFFILIATIONS

Department of Mechanical, Aerospace and Civil Engineering, The University of Manchester, Manchester M13 9PL, United Kingdom

Note: This paper is part of the Special Issue on the Lattice Boltzmann Method.

^{a)}Author to whom correspondence should be addressed: alessandro.derosi@manchester.ac.uk

ABSTRACT

In this paper, a lattice Boltzmann model for the coupled Allen–Cahn–Navier–Stokes equations in three dimensions is presented. Two equations are solved: one for the fluid velocity and one for the order parameter. Both are written within the general multiple-relaxation-time framework, where all the equilibrium and forcing terms are described by using the full set of Hermite polynomials. The resultant practical implementation is compact. The gradient of the order parameter can be computed by the non-local finite differences or the local central moments. The latter suffers from grid-scale oscillations. The very good accuracy properties are demonstrated against nine well-consolidated benchmark tests. Specifically, two groups of tests are tackled. In the former, the velocity field is superimposed. Hence, only the equation for the evolution of the order parameter is solved. These numerical experiments demonstrate the ability of the proposed scheme to capture the correct evolution of the interface. In the latter, two immiscible fluids are considered and the two equations are solved. Simulations of the vertical penetration of a wedge-shaped body, two- and three-dimensional Rayleigh–Taylor instability prove that two-fluids systems can be successfully simulated by our approach.

Published under license by AIP Publishing. <https://doi.org/10.1063/5.0046875>

27 September 2024 08:49:11

NOMENCLATURE

Abbreviations

A-C	Allen-Cahn
BGK	Bhatnagar-Gross-Krook
C-H	Cahn-Hilliard
CFD	computational fluid dynamics
CM	central moment
FD	finite differences
GMRT	general multiple-relaxation time
LBE	lattice Boltzmann equation
LBM	lattice Boltzmann method
Mom	moments
MRT	multiple-relaxation time
N-S	Navier-Stokes
RM	raw moment

Dimensionless numbers

At	Atwood number
Ca	Capillarity number

Ch	Cahn number
Pe	Peclet number
Re	Reynolds number

Superscripts

<i>eq</i>	equilibrium quantity
\star	post-collision quantity
\top	transpose operator

Subscripts

<i>H</i>	heavy fluid
<i>i</i>	index spanning the lattice directions
<i>L</i>	light fluid
ϕ	order parameter-related quantity

Symbols

\bar{c}_i	lattice directions shifted by the local fluid velocity
c_i	lattice directions
c_s	lattice sound speed

F	force vector
f_i	distributions for the velocity field
F_b	external body force
F_p	pressure force
F_s	surface tension force
F_v	viscous force
g_i	distributions for the order parameter
I	unit tensor
k_i	central moments
K	relaxation matrix in the central moments space
L_0	reference length
M	mobility coefficient
M	transformation matrix: populations to raw moments
N	transformation matrix: central moments to raw moments
p	pressure
\tilde{p}	normalized pressure
r_i	raw moments
R_i	central moments of the forcing term
t	time
T	transformation matrix: populations to central moments
\mathbf{u}	velocity vector
U_0	reference velocity
w_i	weighting factors
Λ	relaxation matrix in the population space
μ	dynamic viscosity
μ_ϕ	chemical potential
ν	kinematic viscosity
ξ	interface thickness
ρ	density
σ	surface tension
τ	relaxation time
ϕ	order parameter
ω	relaxation frequency
∇	spatial derivative operator
∇^2	Laplacian operator
$\langle \bullet \rangle$	column vector
$ \bullet\rangle$	row vector

I. INTRODUCTION

The flow of two immiscible incompressible fluids at arbitrary density and viscosity contrasts is commonly experienced in many areas of science and engineering. Their study and application are a key part of multiphase/multicomponent flow solvers in modern computational fluid dynamics (CFD). A popular approach to multiphase CFD is represented by the so-called diffusive interface method,¹ where the interface between the two fluids is represented by a transitional layer with finite thickness across the one fluid properties are continuous and vary smoothly. Diffusive interface methods introduce a continuous phase-field variable (also known as order parameter) to identify and distinguish the different phases/components. The evolution of this quantity can be computed by solving the Cahn–Hilliard equation² or the Allen–Cahn equation.³ Within the traditional CFD based on the solution of the macroscopic Navier–Stokes equations, the phase-field modeling has attracted large attention in recent years leading to finite volume solutions of the C–H and A–C equations coupled to the N–S ones.^{4,5}

Alternatively to the macroscopic-based formulations,^{6–9} the lattice Boltzmann method has become a very powerful approach to simulate the flow of viscous fluids.^{10–12} In short, the LBM idealizes a fluid as collections (also known as distributions or populations) of fictitious particles moving along the links of a fixed Cartesian lattice. These mesoscopic quantities carry with them information about the macroscopic variables (i.e., density and momentum). The widespread adoption of the LBM stems from several advantages. In contrast to Navier–Stokes solvers, which need to treat the non-linear convection term, the LBM does not include such non-linearity. The resultant algorithmic simplicity of the LBM implies an easy coding and allows it to be particularly well-suited for massively parallel computing.¹³ Moreover, the LBM is applicable to simulate multiphase/multicomponent flows due to the possibility to incorporate microscopic interactions.¹⁴ Complex boundaries are easy to deal with using the bounce-back rule and thus the LBM can be applied to simulate flows with complex geometries such as porous media flows.¹⁵ Relevant industrial applications of the LBM cover external aerodynamics, acoustics, and heat transfer. In the last ten years, several companies invested in this technology. The case of Dassault Systems has bought the two popular software XFlow¹⁶ and PowerFLOW.¹⁷ OMNIS/LB by Numeca (a commercial branch of Palabos¹⁸) ProLB by CS,¹⁹ ultraFluidX by Altair, and SimScale are just more recent examples of commercial LBM-based software. Among the rich variety of applications where the LBM has been successfully employed, the simulation of multiphase and multicomponent flows has gained impressive popularity.^{20–22} Aiming at simulating this class of flows, four different approaches can be identified: the color-gradient model,^{23–31} the pseudopotential model,^{32–35} the free energy model^{36–38} and the phase-field approach.^{39–44}

The latter has seen the rise of many recent efforts leading to progressively more sophisticated developments of the theory and numerical implementation. Contributions can be classified into two main groups. The former gathers the works aimed at recovering the C–H equation. In this regard, Zu and He⁴⁵ proposed a scheme with enhanced accuracy and stability with respect to the previous work by Zheng *et al.*⁴⁶ Liang *et al.*^{40,47} developed a multiple-relaxation-time LBM with the introduction of a time derivative in the source term. The latter group develops LBMs for the A–C equation. Specifically, a competitive algorithm was proposed by Geier *et al.*⁴¹ and Fakhari *et al.*⁴³ for two- and three-dimensional simulations, respectively. In these works, the authors argued that the non-local computation of the gradient of the order parameter (see Sec. II for further details) can be avoided because the same quantity can be derived by the local estimation of the first-order central moments. Alternative strategies to perform a local calculation of the gradient of the order parameter were proposed by Wang *et al.*⁴⁸ and Liang *et al.*⁴⁹ Ren *et al.*⁵⁰ proved that the model in Ref. 41 generated artificial terms in the recovered equation. In order to circumvent this problem, they added a time-derivative term. The comparative study by Begmohammadi *et al.*⁵¹ showed that the artificial terms in the model by Geier *et al.*⁴¹ do not dramatically affect the accuracy of the solution, which is in turn roughly similar to the one achieved by the methods in Refs. 48 and 50. Very recently, Zu *et al.*⁵² presented a scheme with very high accuracy properties.

In this paper, we propose a three-dimensional model to solve the coupled Allen–Cahn–Navier–Stokes equations for a system composed of two immiscible incompressible fluids by solving two LBEs through the D3Q19 discretization. Specifically, we derive a general

multiple-relaxation-time framework for both the equations. The resultant collision operators are written in terms of central moments and it is demonstrated that the classical raw-moments-based LBM is a sub-case of the central-moments-based one. Recently, central moments have also been adopted by Gruszczynski *et al.*⁵³ within the framework of the so-called cascaded LBM.⁵⁴ It is also worth noting that an LBM for collision operator in the cumulant space with the decoupled interface tracking for simulations of high Reynolds and Weber regimes has been very recently presented by Hosseini *et al.*⁵⁵ Differently from these works, instead of computing moments of the continuous equilibrium and forcing terms, we adopt the discrete counterparts written with the full set of Hermite polynomials^{56–64} and it results in a compact algorithmic procedure. Interestingly, Dinesh Kumar *et al.*⁶⁵ have developed a phase-field LBM for two immiscible fluids. Differently from this work, our approach uses the full set of Hermite polynomials for all the equilibrium and forcing terms. Moreover, we employ central moments instead of raw ones in the collision operators. Three-dimensional interface tracking LB simulations have been recently carried out by Fakhari *et al.*,⁴³ who built a double-BGK LBM where the velocity space is discretized by seven and fifteen lattice directions. Here, we show that the adoption of nineteen velocities is instrumental to perform more accurate simulations. The approach presented in this paper is tested against nine well-consolidated benchmark problems exhibiting very good accuracy.

The rest of the paper is organized as follows. In Sec. II, our proposed methodology is devised. Results from numerical experiments are presented in Sec. III. Eventually, some conclusions are drawn in Sec. IV.

II. METHODOLOGY

In this section, we first state the macroscopic equations governing the problem. Second, we recall the BGK LBM.^{43,66} Eventually, we present our approach.

A. Problem statement and governing equations

Let us consider a three-dimensional Cartesian space $\mathbf{x} = [x, y, z]$, where x, y and z are the coordinates. The macroscopic behavior of a system composed of two immiscible fluids is governed by the Navier-Stokes equations⁶⁷

$$\begin{aligned} \nabla \cdot \mathbf{u} &= 0, \\ \rho[\partial_t \mathbf{u} + (\mathbf{u} \cdot \nabla) \mathbf{u}] &= -\nabla p + \mu \nabla^2 \mathbf{u} + \mathbf{F}, \end{aligned} \quad (1)$$

where $\mathbf{u} = [u_x, u_y, u_z]$ and $\mathbf{F} = [F_x, F_y, F_z]$. The evolution of the interface between the two fluids is tracked by the conservative form of the Allen-Cahn equation,⁶⁸ that is,

$$\partial_t \phi + \nabla \cdot \phi \mathbf{u} = \nabla \cdot M \left[\nabla \phi - \frac{\nabla \phi}{|\nabla \phi|} \frac{1 - 4(\phi - \phi_0)^2}{\xi} \right], \quad (2)$$

where the order parameter ϕ varies between $\phi_H = 1$ and $\phi_L = 0$. Moreover, the quantity ϕ_0 is defined as $\phi_0 = (\phi_H + \phi_L)/2 = 1/2$. The A-C equation is written by assuming that the interface velocity is split into a normal interface speed and an interface velocity due to external advection. Moreover, the normal interface speed is only proportional to the interface curvature. In addition, the equilibrium phase-field profile for an interface located at $\mathbf{x} = \mathbf{x}_0$ is⁶⁸

$$\phi(\mathbf{x}) = \frac{1}{2} \left[1 - \tanh \left(\frac{2|\mathbf{x} - \mathbf{x}_0|}{\xi} \right) \right]. \quad (3)$$

The problem is governed by the following dimensionless parameters:⁵²

$$\begin{aligned} \text{Re} &= \frac{U_0 L_0}{\nu}, \\ \text{Pe} &= \frac{U_0 L_0}{M}, \\ \text{Ch} &= \frac{\xi}{L_0}. \end{aligned} \quad (4)$$

B. BGK LBM

Let us consider the three-dimensional nineteen-velocities D3Q19 lattice discretization. Two sets of populations are involved in the computations. The former, $|f_i\rangle = [f_0, \dots, f_{18}]^\top$, controls the velocity field, while the latter, $|g_i\rangle = [g_0, \dots, g_{18}]^\top$, monitors the evolution of the order parameter. Distributions move on a fixed Cartesian cubic lattice along the links $i = 0 \dots 18$ with velocity $\mathbf{c}_i = [|c_{xi}\rangle, |c_{yi}\rangle, |c_{zi}\rangle]$ defined as¹¹

$$\begin{aligned} |c_{xi}\rangle &= [0, 1, -1, 0, 0, 0, 1, -1, 1, -1, 1, -1, 0, 0, 0, 0, 0]^\top, \\ |c_{yi}\rangle &= [0, 0, 0, 1, -1, 0, 0, 1, -1, -1, 1, 0, 0, 0, 0, 1, -1, 1, -1]^\top, \\ |c_{zi}\rangle &= [0, 0, 0, 0, 0, 1, -1, 0, 0, 0, 0, 1, -1, -1, 1, 1, -1, -1, 1]^\top. \end{aligned} \quad (5)$$

The governing lattice Boltzmann equations read as follows:¹¹

$$|f_i(\mathbf{x} + \mathbf{c}_i, t + 1)\rangle = |f_i^*(\mathbf{x}, t)\rangle, \quad (6)$$

$$|g_i(\mathbf{x} + \mathbf{c}_i, t + 1)\rangle = |g_i^*(\mathbf{x}, t)\rangle. \quad (7)$$

To lighten the notation, the dependence on space \mathbf{x} and time t will be implicitly assumed in the rest of this section.

Within the BGK approximation,⁶⁹ post-collision populations can be written as

$$f_i^* = f_i + \frac{1}{\tau + 1/2} (f_i^{eq} - f_i) + F_i, \quad (8)$$

$$g_i^* = g_i + \frac{1}{\tau_\phi + 1/2} (g_i^{eq} - g_i) + G_i, \quad (9)$$

where the equilibrium states are⁵³

$$f_i^{eq} = w_i \left[\tilde{p} + \frac{\mathbf{c}_i \cdot \mathbf{u}}{c_s^2} + \frac{(\mathbf{c}_i \cdot \mathbf{u})^2}{2c_s^4} - \frac{\mathbf{u}^2}{2c_s^2} \right], \quad (10)$$

$$g_i^{eq} = w_i \phi \left[1 + \frac{\mathbf{c}_i \cdot \mathbf{u}}{c_s^2} + \frac{(\mathbf{c}_i \cdot \mathbf{u})^2}{2c_s^4} - \frac{\mathbf{u}^2}{2c_s^2} \right] \quad (11)$$

$\tilde{p} = p/(\rho c_s^2)$ being the normalized pressure. Weighting factors are $w_0 = 1/3$, $w_{1\dots 6} = 1/18$ and $w_{7\dots 18} = 1/36$. The lattice sound speed is $c_s = 1/\sqrt{3}$.¹¹ The relaxation times are evaluated as

$$\tau = \tau_L + \frac{\phi - \phi_L}{\phi_H - \phi_L} (\tau_H - \tau_L), \quad (12)$$

$$\tau_\phi = \frac{M}{c_s^2}, \quad (13)$$

where $\tau_L = \mu_L/(\rho c_s^2)$ and $\tau_H = \mu_H/(\rho c_s^2)$ are the relaxation times associated with the dynamic viscosities of the light and heavy fluids, respectively.⁵³

The two forcing terms are⁴²

$$F_i = w_i \frac{\mathbf{c}_i \cdot \mathbf{F}}{\rho c_s^2}, \quad (14)$$

$$G_i = w_i \frac{\mathbf{c}_i \cdot \mathbf{F}_\phi}{c_s^2}, \quad (15)$$

where

$$\mathbf{F}_\phi = [F_{x,\phi}, F_{y,\phi}, F_{z,\phi}] = c_s^2 \frac{1 - 4(\phi - \phi_0)^2}{\xi} \cdot \frac{\nabla \phi}{|\nabla \phi|}. \quad (16)$$

The force \mathbf{F} gathers four contributions⁴²

$$\mathbf{F} = \mathbf{F}_s + \mathbf{F}_p + \mathbf{F}_\nu + \mathbf{F}_b. \quad (17)$$

\mathbf{F}_s accounts for the surface tension σ as

$$\mathbf{F}_s = \mu_\phi \nabla \phi \quad (18)$$

with the chemical potential

$$\mu_\phi = 4\beta(\phi - \phi_L)(\phi - \phi_H)(\phi - \phi_0) - \kappa \nabla^2 \phi, \quad (19)$$

where $\beta = 12\sigma/\xi$ and $\kappa = 3\sigma\xi/2$.⁴² Gradient and Laplacian of ϕ can be computed by isotropic finite differences (FD)⁷⁰

$$\nabla \phi = \frac{1}{c_s^2} \sum_i w_i \mathbf{c}_i \phi(\mathbf{x} + \mathbf{c}_i), \quad (20)$$

$$\nabla^2 \phi = \frac{2}{c_s^2} \sum_i w_i [\phi(\mathbf{x} + \mathbf{c}_i) - \phi(\mathbf{x})]. \quad (21)$$

The same formulas apply to estimate the spatial derivatives of any other quantity. Pressure and viscous forces are

$$\begin{aligned} \mathbf{F}_p &= -\tilde{p} c_s^2 \nabla \rho, \\ \mathbf{F}_\nu &= \nu \left[\nabla \mathbf{u} + (\nabla \mathbf{u})^\top \right] \cdot \nabla \rho, \end{aligned} \quad (22)$$

respectively, where the fluid kinematic viscosity is $\nu = \tau c_s^2$. The gradient of density is determined based on the gradient of the order parameter,⁵³ that is,

$$\nabla \rho = \frac{\rho_H - \rho_L}{\phi_H - \phi_L} \nabla \phi. \quad (23)$$

The last term, \mathbf{F}_b , accounts for a generic body force (e.g., gravity).

Macroscopic variables are readily available as⁵³

$$\begin{aligned} \tilde{p} &= \sum_i f_i, \\ \mathbf{u} &= \sum_i f_i \mathbf{c}_i + \frac{\mathbf{F}}{2\rho}, \\ \phi &= \sum_i g_i. \end{aligned} \quad (24)$$

The fluid density ρ is computed by a linear interpolation,⁵³ that is,

$$\rho = \rho_L + \frac{\phi - \phi_L}{\phi_H - \phi_L} (\rho_H - \rho_L). \quad (25)$$

C. 3D GMRT-LBM for f_i

Before deriving the general multiple-relaxation-time LBM for the evolution of the velocity field, it is of interest to underline that Eq. (10) is the well-known second-order truncated expression of the equilibrium state. However, several authors demonstrated that the full potential of any LB discretization (in terms of physical and numerical properties) can only be achieved by using the complete allowable set of

Hermite polynomials.^{56,57,71–73} Following Coreixas *et al.*⁷² and De Rosis and Coreixas,⁷⁴ we propose to rewrite Eq. (10) as:

$$f_{(0,0,0)}^{eq} = \frac{1}{3} [\tilde{p} - (u_x^2 + u_y^2 + u_z^2) + 3(u_x^2 u_y^2 + u_x^2 u_z^2 + u_y^2 u_z^2)],$$

$$f_{(\psi,0,0)}^{eq} = \frac{1}{18} [\tilde{p} + 3\psi u_x + 3(u_x^2 - u_y^2 - u_z^2) - 9\psi(u_x u_y^2 + u_x u_z^2) - 9(u_x^2 u_y^2 + u_x^2 u_z^2)],$$

$$f_{(0,\lambda,0)}^{eq} = \frac{1}{18} [\tilde{p} + 3\lambda u_y + 3(-u_x^2 + u_y^2 - u_z^2) - 9\lambda(u_x^2 u_y + u_y u_z^2) - 9(u_x^2 u_y^2 + u_y^2 u_z^2)],$$

$$\begin{aligned} f_{(\psi,\lambda,0)}^{eq} &= \frac{1}{36} [\tilde{p} + 3(\psi u_x + \lambda u_y) + 3(u_x^2 + u_y^2) + 9\psi\lambda u_x u_y \\ &\quad + 9(\lambda u_x^2 u_y + \psi u_x u_y^2) + 9u_x^2 u_y^2], \end{aligned}$$

$$\begin{aligned} f_{(\psi,0,\lambda)}^{eq} &= \frac{1}{36} [\tilde{p} + 3(\psi u_x + \chi u_z) + 3(u_x^2 + u_z^2) + 9\psi\chi u_x u_z \\ &\quad + 9(\chi u_x^2 u_z + \psi u_x u_z^2) + 9u_x^2 u_z^2], \\ f_{(0,\lambda,\lambda)}^{eq} &= \frac{1}{36} [\tilde{p} + 3(\lambda u_y + \chi u_z) + 3(u_y^2 + u_z^2) + 9\lambda\chi u_y u_z \\ &\quad + 9(\chi u_y^2 u_z + \lambda u_y u_z^2) + 9u_y^2 u_z^2], \end{aligned} \quad (26)$$

where $(\psi, \lambda, \chi) \in \{\pm 1\}^3$ and the tensor product notation has been adopted for the sake of compactness.^{75–77}

After this premise, let us express the LBE with the forcing term as [(76) and (77)]

$$\begin{aligned} |f_i(\mathbf{x} + \mathbf{c}_i, t + 1)\rangle &= |f_i(\mathbf{x}, t)\rangle + \Lambda [|f_i^{eq}(\mathbf{x}, t)\rangle - |f_i(\mathbf{x}, t)\rangle] \\ &\quad + (\mathbf{I} - \Lambda/2) |F_i(\mathbf{x}, t)\rangle. \end{aligned} \quad (27)$$

Equation (27) collapses into the aforementioned BGK LBM if the collision matrix is set to $\Lambda = \omega \mathbf{I}$, where \mathbf{I} is the unit tensor and $\omega = \frac{1}{t+1/2}$ is the relaxation frequency. The term F_i accounts for external body forces \mathbf{F} and its prefactor is responsible for the discrete effects originating from the change of variables that aims at obtaining a numerical scheme explicit in time.⁷⁸ As usual, the LBE can be divided into two steps, which are collision

$$\begin{aligned} |f_i^*(\mathbf{x}, t)\rangle &= |f_i(\mathbf{x}, t)\rangle + \Lambda [|f_i^{eq}(\mathbf{x}, t)\rangle - |f_i(\mathbf{x}, t)\rangle] \\ &\quad + (\mathbf{I} - \Lambda/2) |F_i(\mathbf{x}, t)\rangle \end{aligned} \quad (28)$$

and streaming

$$|f_i(\mathbf{x} + \mathbf{c}_i, t + 1)\rangle = |f_i^*(\mathbf{x}, t)\rangle. \quad (29)$$

Let us first neglect the presence of F_i . In order to build a CMs-based collision operator, the lattice directions are shifted by the local fluid velocity (54). These shifted discrete velocities $\bar{\mathbf{c}}_i = [\langle \bar{c}_{ix} \rangle, \langle \bar{c}_{iy} \rangle, \langle \bar{c}_{iz} \rangle]$ are defined as

$$\begin{aligned} \langle \bar{c}_{ix} \rangle &= \langle c_{ix} - u_x \rangle, \\ \langle \bar{c}_{iy} \rangle &= \langle c_{iy} - u_y \rangle, \\ \langle \bar{c}_{iz} \rangle &= \langle c_{iz} - u_z \rangle. \end{aligned} \quad (30)$$

Populations are transformed into central moments by applying the following transformation matrix \mathbf{T} :⁷⁴

$$\mathbf{T} = \begin{bmatrix} \langle |\mathbf{c}_i|^0 | \\ \langle \bar{c}_{ix} | \\ \langle \bar{c}_{iy} | \\ \langle \bar{c}_{iz} | \\ \langle \bar{c}_{ix}^2 + \bar{c}_{iy}^2 + \bar{c}_{iz}^2 | \\ \langle \bar{c}_{ix}^2 - \bar{c}_{iy}^2 | \\ \langle \bar{c}_{iy}^2 - \bar{c}_{iz}^2 | \\ \langle \bar{c}_{ix}\bar{c}_{iy} | \\ \langle \bar{c}_{ix}\bar{c}_{iz} | \\ \langle \bar{c}_{iy}\bar{c}_{iz} | \\ \langle \bar{c}_{ix}\bar{c}_{iy}^2 | \\ \langle \bar{c}_{ix}\bar{c}_{iz}^2 | \\ \langle \bar{c}_{iy}\bar{c}_{iz}^2 | \\ \langle \bar{c}_{ix}^2\bar{c}_{iy}^2 | \\ \langle \bar{c}_{ix}^2\bar{c}_{iz}^2 | \\ \langle \bar{c}_{iy}^2\bar{c}_{iz}^2 | \\ \langle \bar{c}_{iy}\bar{c}_{iz}^2 | \end{bmatrix}. \quad (31)$$

This basis directly flows from its D3Q27 counterpart where monomials related to discrete velocities $(\pm 1, \pm 1, \pm 1)$ are discarded.^{72,79} The relaxation matrix in the populations space then is $\Lambda = \mathbf{T}^{-1}\mathbf{K}\mathbf{T}$, where $\mathbf{K} = \text{diag}[1, 1, 1, 1, 1, \omega, \omega, \omega, \omega, \omega, 1, \dots, 1]$ is the 19×19 relaxation matrix in the CMs space.

Let us collect pre-collision, equilibrium and post-collision CMs as

$$\begin{aligned} |k_i\rangle &= [k_0, \dots, k_i, \dots, k_{18}]^\top, \\ |k_i^{\text{eq}}\rangle &= [k_0^{\text{eq}}, \dots, k_i^{\text{eq}}, \dots, k_{18}^{\text{eq}}]^\top, \\ |k_i^*\rangle &= [k_0^*, \dots, k_i^*, \dots, k_{18}^*]^\top, \end{aligned} \quad (32)$$

respectively. The first two quantities are evaluated by applying the matrix \mathbf{T} to the corresponding distributions as

$$\begin{aligned} |k_i\rangle &= \mathbf{T}|f_i\rangle, \\ |k_i^{\text{eq}}\rangle &= \mathbf{T}|f_i^{\text{eq}}\rangle. \end{aligned} \quad (33)$$

As a consequence, equilibrium CMs read as follows:

$$\begin{aligned} k_0^{\text{eq}} &= \tilde{p}, \\ k_1^{\text{eq}} &= -u_x(\tilde{p} - 1), \\ k_2^{\text{eq}} &= -u_y(\tilde{p} - 1), \\ k_3^{\text{eq}} &= -u_z(\tilde{p} - 1), \\ k_4^{\text{eq}} &= (u_x^2 + u_y^2 + u_z^2)(\tilde{p} - 1), \\ k_5^{\text{eq}} &= (u_x^2 - u_y^2)(\tilde{p} - 1), \\ k_6^{\text{eq}} &= (u_y^2 - u_z^2)(\tilde{p} - 1), \\ k_7^{\text{eq}} &= u_x u_y (\tilde{p} - 1), \\ k_8^{\text{eq}} &= u_x u_z (\tilde{p} - 1), \\ k_9^{\text{eq}} &= u_y u_z (\tilde{p} - 1), \\ k_{10}^{\text{eq}} &= -u_y(3u_x^2 + 1)(\tilde{p} - 1)c_s^2, \\ k_{11}^{\text{eq}} &= -u_x(3u_y^2 + 1)(\tilde{p} - 1)c_s^2, \\ k_{12}^{\text{eq}} &= -u_z(3u_x^2 + 1)(\tilde{p} - 1)c_s^2, \\ k_{13}^{\text{eq}} &= -u_x(3u_z^2 + 1)(\tilde{p} - 1)c_s^2, \\ k_{14}^{\text{eq}} &= -u_z(3u_y^2 + 1)(\tilde{p} - 1)c_s^2, \\ k_{15}^{\text{eq}} &= -u_y(3u_z^2 + 1)(\tilde{p} - 1)c_s^2, \\ k_{16}^{\text{eq}} &= \tilde{p} [c_s^4 + c_s^2(u_x^2 + u_y^2) + u_x^2 u_y^2] - c_s^2(u_x^2 + u_y^2) - u_x^2 u_y^2, \\ k_{17}^{\text{eq}} &= \tilde{p} [c_s^4 + c_s^2(u_x^2 + u_z^2) + u_x^2 u_z^2] - c_s^2(u_x^2 + u_z^2) - u_x^2 u_z^2, \\ k_{18}^{\text{eq}} &= \tilde{p} [c_s^4 + c_s^2(u_y^2 + u_z^2) + u_y^2 u_z^2] - c_s^2(u_y^2 + u_z^2) - u_y^2 u_z^2. \end{aligned} \quad (34)$$

These expressions degrade into the ones obtained by De Rosis and Coreixas⁷⁴ for a single-phase fluid system when $p = \rho c_s^2$. The collision process is given by

$$\begin{aligned} |k_i^*\rangle &= (\mathbf{I} - \mathbf{K})\mathbf{T}|f_i\rangle + \mathbf{K}\mathbf{T}|f_i^{\text{eq}}\rangle, \\ &= (\mathbf{I} - \mathbf{K})|k_i\rangle + \mathbf{K}|k_i^{\text{eq}}\rangle. \end{aligned} \quad (35)$$

After the collision, CMs are

$$\begin{aligned} k_0^* &= \tilde{p}, \\ k_1^* &= -u_x(\tilde{p} - 1), \\ k_2^* &= -u_y(\tilde{p} - 1), \\ k_3^* &= -u_z(\tilde{p} - 1), \\ k_4^* &= (u_x^2 + u_y^2 + u_z^2)(\tilde{p} - 1), \\ k_5^* &= (1 - \omega)k_5 + \omega(u_x^2 - u_y^2)(\tilde{p} - 1), \\ k_6^* &= (1 - \omega)k_6 + \omega(u_y^2 - u_z^2)(\tilde{p} - 1), \\ k_7^* &= (1 - \omega)k_7 + \omega u_x u_y (\tilde{p} - 1), \\ k_8^* &= (1 - \omega)k_8 + \omega u_x u_z (\tilde{p} - 1), \\ k_9^* &= (1 - \omega)k_9 + \omega u_y u_z (\tilde{p} - 1), \\ k_{10}^* &= -u_y(3u_x^2 + 1)(\tilde{p} - 1)c_s^2, \\ k_{11}^* &= -u_x(3u_y^2 + 1)(\tilde{p} - 1)c_s^2, \\ k_{12}^* &= -u_z(3u_x^2 + 1)(\tilde{p} - 1)c_s^2, \\ k_{13}^* &= -u_x(3u_z^2 + 1)(\tilde{p} - 1)c_s^2, \\ k_{14}^* &= -u_z(3u_y^2 + 1)(\tilde{p} - 1)c_s^2, \\ k_{15}^* &= -u_y(3u_z^2 + 1)(\tilde{p} - 1)c_s^2, \\ k_{16}^* &= \tilde{p} [c_s^4 + c_s^2(u_x^2 + u_y^2) + u_x^2 u_y^2] - c_s^2(u_x^2 + u_y^2) - u_x^2 u_y^2, \\ k_{17}^* &= \tilde{p} [c_s^4 + c_s^2(u_x^2 + u_z^2) + u_x^2 u_z^2] - c_s^2(u_x^2 + u_z^2) - u_x^2 u_z^2, \\ k_{18}^* &= \tilde{p} [c_s^4 + c_s^2(u_y^2 + u_z^2) + u_y^2 u_z^2] - c_s^2(u_y^2 + u_z^2) - u_y^2 u_z^2, \end{aligned} \quad (36)$$

where pre-collision CMs can be computed as

$$k_5 = \sum_i f_i (\bar{c}_{ix}^2 - \bar{c}_{iy}^2),$$

$$\begin{aligned} k_6 &= \sum_i f_i (\bar{c}_{iy}^2 - \bar{c}_{iz}^2), \\ k_7 &= \sum_i f_i \bar{c}_{ix} \bar{c}_{iy}, \\ k_8 &= \sum_i f_i \bar{c}_{ix} \bar{c}_{iz}, \\ k_9 &= \sum_i f_i \bar{c}_{iy} \bar{c}_{iz}. \end{aligned} \quad (37)$$

These quantities can be rewritten as

$$\begin{aligned} k_5 &= r_5 + (u_x^2 - u_y^2)(\tilde{p} - 2), \\ k_6 &= r_6 + (u_y^2 - u_z^2)(\tilde{p} - 2), \\ k_7 &= r_7 + u_x u_y (\tilde{p} - 2), \\ k_8 &= r_8 + u_x u_z (\tilde{p} - 2), \\ k_9 &= r_9 + u_y u_z (\tilde{p} - 2), \end{aligned} \quad (38)$$

where pre-collision raw moments are

$$\begin{aligned} r_5 &= \sum_i f_i (c_{ix}^2 - c_{iy}^2) = f_1 + f_2 - f_3 - f_4 + f_{11} \\ &\quad + f_{12} + f_{13} + f_{14} - f_{15} - f_{16} - f_{17} - f_{18}, \\ r_6 &= \sum_i f_i (c_{iy}^2 - c_{iz}^2) = f_3 + f_4 - f_5 - f_6 + f_7 \\ &\quad + f_8 + f_9 + f_{10} - f_{11} - f_{12} - f_{13} - f_{14}, \\ r_7 &= \sum_i f_i c_{ix} c_{iy} = f_7 + f_8 - f_9 - f_{10}, \\ r_8 &= \sum_i f_i c_{ix} c_{iz} = f_{11} + f_{12} - f_{13} - f_{14}, \\ r_9 &= \sum_i f_i c_{iy} c_{iz} = f_{15} + f_{16} - f_{17} - f_{18}. \end{aligned} \quad (39)$$

We are now in the position to reconstruct post-collision populations as

$$|f_i^* \rangle = \mathbf{T}^{-1} |k_i^* \rangle, \quad (40)$$

with $|f_i^* \rangle = [f_0^*, \dots, f_i^*, \dots, f_{18}]^\top$. Eventually, populations are streamed by Eq. (6) and macroscopic variables are computed by Eq. (24).

In the presence of external forces, post-collision CMs then read as

$$\begin{aligned} |k_i^* \rangle &= (\mathbf{I} - \mathbf{K}) \mathbf{T} |f_i \rangle + \mathbf{K} \mathbf{T} |f_i^{\text{eq}} \rangle + \left(\mathbf{I} - \frac{\mathbf{K}}{2} \right) \mathbf{T} |F_i \rangle \\ &= (\mathbf{I} - \mathbf{K}) |k_i \rangle + \mathbf{K} |k_i^{\text{eq}} \rangle + \left(\mathbf{I} - \frac{\mathbf{K}}{2} \right) |R_i \rangle, \end{aligned} \quad (41)$$

where

$$|R_i \rangle = \mathbf{T} |F_i \rangle \quad (42)$$

is the vector collecting the central moments of the forcing term. Its components are⁷⁴

$$\begin{aligned} R_0 &= 0, \\ R_1 &= F_x, \\ R_2 &= F_y, \\ R_3 &= F_z, \\ R_4 &= 0, \end{aligned}$$

$$\begin{aligned} R_5 &= 0, \\ R_6 &= 0, \\ R_7 &= 0, \\ R_8 &= 0, \\ R_9 &= 0, \\ R_{10} &= F_y c_s^2, \\ R_{11} &= F_x c_s^2, \\ R_{12} &= F_z c_s^2, \\ R_{13} &= F_x c_s^2, \\ R_{14} &= F_z c_s^2, \\ R_{15} &= F_y c_s^2, \\ R_{16} &= 0, \\ R_{17} &= 0, \\ R_{18} &= 0. \end{aligned} \quad (43)$$

Interestingly, only nine out of nineteen components are non-zero. Eventually, post-collision CMs are corrected and their expressions are given in Eq. (A9).

Instead of solving Eq. (40), it is more convenient to transform post-collision central moments into post-collision raw moments.⁷⁹ This can be done by decomposing the matrix \mathbf{T} into the product of two matrices, i.e., $\mathbf{T} = \mathbf{M} \mathbf{N}$. The former contribution is built similarly to Eq. (31), but without shifting the lattice directions by the local fluid velocity. Hence, it transforms populations into raw moments. The latter is a lower triangular shifting matrix that converts central moments into raw ones.⁸⁰ Post-collision populations become⁸⁰

$$|f_i^* \rangle = \mathbf{M}^{-1} \mathbf{N}^{-1} |k_i^* \rangle. \quad (44)$$

First, post-collision raw moments are computed as

$$|r_i^* \rangle = \mathbf{N}^{-1} |k_i^* \rangle. \quad (45)$$

Their expressions are not reported herein because they might be too tedious. However, the interested reader can find the script D3Q19-CentralMoments-PhaseField.m in the [supplementary material](#), where all the symbolic manipulations to derive the models presented in this paper can be performed. Then, post-collision populations can be constructed as

$$|f_i^* \rangle = \mathbf{M}^{-1} |r_i^* \rangle. \quad (46)$$

These are equal to

$$\begin{aligned} f_0^* &= r_0^* - r_4^* + r_{16}^* + r_{17}^* + r_{18}^*, \\ f_1^* &= (r_4^* + 2r_5^* + r_6^*) c_s^2 / 2 - (-r_1^* + r_{11}^* + r_{13}^* + r_{16}^* + r_{17}^*) / 2, \\ f_2^* &= (r_4^* + 2r_5^* + r_6^*) c_s^2 / 2 + (r_{11}^* + r_{13}^* - r_1^* - r_{16}^* - r_{17}^*) / 2, \\ f_3^* &= (r_4^* - r_5^* + r_6^*) c_s^2 / 2 - (-r_2^* + r_{10}^* + r_{15}^* + r_{16}^* + r_{18}^*) / 2, \\ f_4^* &= (r_4^* - r_5^* + r_6^*) c_s^2 / 2 - (r_2^* - r_{10}^* - r_{15}^* + r_{16}^* + r_{18}^*) / 2, \\ f_5^* &= (r_4^* - r_5^* - 2r_6^*) c_s^2 / 2 - (-r_3^* + r_{12}^* + r_{14}^* + r_{17}^* + r_{18}^*) / 2, \\ f_6^* &= (r_4^* - r_5^* - 2r_6^*) c_s^2 / 2 - (r_3^* - r_{12}^* - r_{14}^* + r_{17}^* + r_{18}^*) / 2, \\ f_7^* &= (r_7^* + r_{10}^* + r_{11}^* + r_{16}^*) / 4, \\ f_8^* &= (r_7^* + r_{16}^* - r_{10}^* - r_{11}^*) / 4, \\ f_9^* &= (r_{11}^* + r_{16}^* - r_7^* - r_{10}^*) / 4, \end{aligned}$$

$$\begin{aligned}
f_{10}^* &= (r_{10}^* + r_{16}^* - r_7^* - r_{11}^*)/4, \\
f_{11}^* &= (r_8^* + r_{12}^* + r_{13}^* + r_{17}^*)/4, \\
f_{12}^* &= (r_8^* + r_{17}^* - r_{12}^* - r_{13}^*)/4, \\
f_{13}^* &= (r_{13}^* + r_{17}^* - r_8^* - r_{12}^*)/4, \\
f_{14}^* &= (r_{12}^* + r_{17}^* - r_8^* - r_{13}^*)/4, \\
f_{15}^* &= (r_9^* + r_{14}^* + r_{15}^* + r_{18}^*)/4, \\
f_{16}^* &= (r_9^* + r_{18}^* - r_{14}^* - r_{15}^*)/4, \\
f_{17}^* &= (r_{15}^* + r_{18}^* - r_9^* - r_{14}^*)/4, \\
f_{18}^* &= (r_{14}^* + r_{18}^* - r_9^* - r_{15}^*)/4.
\end{aligned} \tag{47}$$

It is of interest to highlight that the classical multiple-relaxation-time LBM based on the relaxation of raw moments can be derived from the above-outlined formulation by simply setting $T = M$ (i.e., by neglecting the role of the shifting matrix N). In the RMs-based LBM, equilibrium and post-collision RMs are

$$\begin{aligned}
r_0^{eq} &= \tilde{p}, \\
r_1^{eq} &= u_x, \\
r_2^{eq} &= u_y, \\
r_3^{eq} &= u_z, \\
r_4^{eq} &= u_x^2 + u_y^2 + u_z^2 + \tilde{p}, \\
r_5^{eq} &= u_x^2 - u_y^2, \\
r_6^{eq} &= u_y^2 - u_z^2, \\
r_7^{eq} &= u_x u_y, \\
r_8^{eq} &= u_x u_z, \\
r_9^{eq} &= u_y u_z, \\
r_{10}^{eq} &= u_y(u_x^2 + c_s^2), \\
r_{11}^{eq} &= u_x(u_y^2 + c_s^2), \\
r_{12}^{eq} &= u_z(u_x^2 + c_s^2), \\
r_{13}^{eq} &= u_x(u_z^2 + c_s^2), \\
r_{14}^{eq} &= u_z(u_y^2 + c_s^2), \\
r_{15}^{eq} &= u_y(u_z^2 + c_s^2), \\
r_{16}^{eq} &= u_x^2 u_y^2 + c_s^2(u_x^2 + u_y^2) + \tilde{p} c_s^4, \\
r_{17}^{eq} &= u_x^2 u_z^2 + c_s^2(u_x^2 + u_z^2) + \tilde{p} c_s^4, \\
r_{18}^{eq} &= u_y^2 u_z^2 + c_s^2(u_y^2 + u_z^2) + \tilde{p} c_s^4
\end{aligned} \tag{48}$$

and

$$\begin{aligned}
r_0^* &= \tilde{p}, \\
r_1^* &= F_x/2 + u_x, \\
r_2^* &= F_y/2 + u_y, \\
r_3^* &= F_z/2 + u_z, \\
r_4^* &= u_x^2 + u_y^2 + u_z^2 + \tilde{p}, \\
r_5^* &= (1 - \omega)r_5 + \omega(u_x^2 - u_y^2), \\
r_6^* &= (1 - \omega)r_6 + \omega(u_y^2 - u_z^2), \\
r_7^* &= (1 - \omega)r_7 + \omega u_x u_y, \\
r_8^* &= (1 - \omega)r_8 + \omega u_x u_z, \\
r_9^* &= (1 - \omega)r_9 + \omega u_y u_z,
\end{aligned}$$

$$\begin{aligned}
r_{10}^* &= F_y c_s^2 / 2 + u_y(u_x^2 + c_s^2), \\
r_{11}^* &= F_x c_s^2 / 2 + u_x(u_y^2 + c_s^2), \\
r_{12}^* &= F_z c_s^2 / 2 + u_z(u_x^2 + c_s^2), \\
r_{13}^* &= F_x c_s^2 / 2 + u_x(u_z^2 + c_s^2), \\
r_{14}^* &= F_z c_s^2 / 2 + u_z(u_y^2 + c_s^2), \\
r_{15}^* &= F_y c_s^2 / 2 + u_y(u_z^2 + c_s^2), \\
r_{16}^* &= u_x^2 u_y^2 + c_s^2(u_x^2 + u_y^2) + \tilde{p} c_s^4, \\
r_{17}^* &= u_x^2 u_z^2 + c_s^2(u_x^2 + u_z^2) + \tilde{p} c_s^4, \\
r_{18}^* &= u_y^2 u_z^2 + c_s^2(u_y^2 + u_z^2) + \tilde{p} c_s^4,
\end{aligned} \tag{49}$$

respectively. Eventually, post-collision populations can be again obtained by Eq. (47) and streamed by the usual Eq. (6).

D. 3D GMRT-LBM for \mathbf{g}_i

Analogously to the actions taken for f_i , we propose to rewrite the equilibrium state in Eq. (11) by adopting the full set of Hermite polynomials. The resultant expressions are

$$\begin{aligned}
g_{(0,0,0)}^{eq} &= \frac{\phi}{3}[1 - (u_x^2 + u_y^2 + u_z^2) + 3(u_x^2 u_y^2 + u_x^2 u_z^2 + u_y^2 u_z^2)], \\
g_{(\psi,0,0)}^{eq} &= \frac{\phi}{18}[1 + 3\psi u_x + 3(u_x^2 - u_y^2 - u_z^2) \\
&\quad - 9\psi(u_x u_y^2 + u_x u_z^2) - 9(u_x^2 u_y^2 + u_x^2 u_z^2)], \\
g_{(0,\lambda,0)}^{eq} &= \frac{\phi}{18}[1 + 3\lambda u_y + 3(-u_x^2 + u_y^2 - u_z^2) \\
&\quad - 9\lambda(u_x^2 u_y + u_y^2 u_z) - 9(u_x^2 u_y^2 + u_y^2 u_z^2)], \\
g_{(0,0,\chi)}^{eq} &= \frac{\phi}{18}[1 + 3\chi u_z + 3(-u_x^2 - u_y^2 + u_z^2) \\
&\quad - 9\chi(u_x^2 u_z + u_y^2 u_z) - 9(u_x^2 u_z^2 + u_y^2 u_z^2)], \\
g_{(\psi,\lambda,0)}^{eq} &= \frac{\phi}{36}[1 + 3(\psi u_x + \lambda u_y) + 3(u_x^2 + u_y^2) \\
&\quad + 9\psi\lambda u_x u_y + 9(\lambda u_x^2 u_y + \psi u_x u_y^2) + 9u_x^2 u_y^2], \\
g_{(\psi,0,\chi)}^{eq} &= \frac{\phi}{36}[1 + 3(\psi u_x + \chi u_z) + 3(u_x^2 + u_z^2) + 9\psi\chi u_x u_z \\
&\quad + 9(\chi u_x^2 u_z + \psi u_x u_z^2) + 9u_x^2 u_z^2], \\
g_{(0,\lambda,\chi)}^{eq} &= \frac{\phi}{36}[1 + 3(\lambda u_y + \chi u_z) + 3(u_y^2 + u_z^2) + 9\lambda\chi u_y u_z \\
&\quad + 9(\chi u_y^2 u_z + \lambda u_y u_z^2) + 9u_y^2 u_z^2].
\end{aligned} \tag{50}$$

The collision stage performed in the space of central moments is

$$\begin{aligned}
|k_{i,\phi}^*\rangle &= (\mathbf{I} - \mathbf{K}_\phi)\mathbf{T}|g_i\rangle + \mathbf{K}_\phi\mathbf{T}|g_i^{eq}\rangle + \left(\mathbf{I} - \frac{\mathbf{K}_\phi}{2}\right)\mathbf{T}|G_i\rangle \\
&= (\mathbf{I} - \mathbf{K}_\phi)|k_{i,\phi}\rangle + \mathbf{K}_\phi|k_{i,\phi}^{eq}\rangle + \left(\mathbf{I} - \frac{\mathbf{K}_\phi}{2}\right)|R_{i,\phi}\rangle,
\end{aligned} \tag{51}$$

where vectors $|k_{i,\phi}\rangle$, $|k_{i,\phi}^{eq}\rangle$ and $|R_{i,\phi}\rangle$ gather pre-collision, equilibrium, and post-collision as

$$\begin{aligned} |k_{i,\phi}\rangle &= [k_{0,\phi}, \dots, k_{i,\phi}, \dots, k_{18,\phi}]^\top, \\ |k_{i,\phi}^{\text{eq}}\rangle &= [k_{0,\phi}^{\text{eq}}, \dots, k_{i,\phi}^{\text{eq}}, \dots, k_{18,\phi}^{\text{eq}}]^\top, \\ |k_{i,\phi}^*\rangle &= [k_{0,\phi}^*, \dots, k_{i,\phi}^*, \dots, k_{18,\phi}^*]^\top, \end{aligned} \quad (52)$$

respectively. The first two quantities are obtained as

$$\begin{aligned} |k_{i,\phi}\rangle &= \mathbf{T}|g_i\rangle, \\ |k_{i,\phi}^{\text{eq}}\rangle &= \mathbf{T}|g_i^{\text{eq}}\rangle. \end{aligned} \quad (53)$$

Interestingly, only five equilibrium CMs are different from zero

$$\begin{aligned} k_{0,\phi}^{\text{eq}} &= \phi, \\ k_{4,\phi}^{\text{eq}} &= \phi, \\ k_{16,\phi}^{\text{eq}} &= \phi c_s^4, \\ k_{17,\phi}^{\text{eq}} &= \phi c_s^4, \\ k_{18,\phi}^{\text{eq}} &= \phi c_s^4. \end{aligned} \quad (54)$$

Before going any further, it should be noted that this equilibrium state is equivalent to the one obtained by De Rosis and Coreixas⁷⁴ with the only difference that now ϕ replaces ρ . This clearly derives from the fact that ϕ replaces ρ in Eq. (50) too. Moreover, equilibrium CMs show elegant and Galilean invariant (i.e., velocity-independent) expressions. This is consistent with the analysis carried out by De Rosis and Luo⁵⁸ for the D3Q27 space, where it was demonstrated that Galilean invariant equilibrium central moments can be obtained only when the transformation matrix is applied to the equilibrium populations written with the complete basis of Hermite polynomials, as done in the present formulation.

By adopting the 19×19 relaxation matrix

$$\mathbf{K}_\phi = \text{diag}[1, \omega_\phi, \omega_\phi, \omega_\phi, 1, \dots, 1] \quad (55)$$

the post-collision state in terms of central moments is

$$\begin{aligned} k_{0,\phi}^* &= \phi, \\ k_{1,\phi}^* &= (1 - \omega_\phi)k_{1,\phi}, \\ k_{2,\phi}^* &= (1 - \omega_\phi)k_{2,\phi}, \\ k_{3,\phi}^* &= (1 - \omega_\phi)k_{3,\phi}, \\ k_{4,\phi}^* &= \phi, \\ k_{10,\phi}^* &= 0, \\ k_{11,\phi}^* &= 0, \\ k_{12,\phi}^* &= 0, \\ k_{13,\phi}^* &= 0, \\ k_{14,\phi}^* &= 0, \\ k_{15,\phi}^* &= 0, \\ k_{16,\phi}^* &= \phi c_s^4, \\ k_{17,\phi}^* &= \phi c_s^4, \\ k_{18,\phi}^* &= \phi c_s^4, \end{aligned} \quad (56)$$

where $\omega_\phi = \frac{1}{\tau_\phi + 1/2}$. The required pre-collision central moments are

$$\begin{aligned} k_{1,\phi} &= \sum_i g_i \bar{c}_{ix}, \\ k_{2,\phi} &= \sum_i g_i \bar{c}_{iy}, \\ k_{3,\phi} &= \sum_i g_i \bar{c}_{iz}, \end{aligned} \quad (57)$$

which can be computed as

$$\begin{aligned} k_{1,\phi} &= r_{1,\phi} - \phi u_x, \\ k_{2,\phi} &= r_{2,\phi} - \phi u_y, \\ k_{3,\phi} &= r_{3,\phi} - \phi u_z, \end{aligned} \quad (58)$$

where pre-collision raw moments are

$$\begin{aligned} r_{1,\phi} &= \sum_i g_i c_{ix} = g_1 - g_2 + g_7 - g_8 + g_9 - g_{10} + g_{11} - g_{12} + g_{13} - g_{14}, \\ r_{2,\phi} &= \sum_i g_i c_{iy} = g_3 - g_4 + g_7 - g_8 - g_9 + g_{10} + g_{15} - g_{16} + g_{17} - g_{18}, \\ r_{3,\phi} &= \sum_i g_i c_{iz} = g_5 - g_6 + g_{11} - g_{12} - g_{13} + g_{14} + g_{15} - g_{16} - g_{17} + g_{18}. \end{aligned} \quad (59)$$

The forcing term is

$$|R_{i,\phi}\rangle = \mathbf{T}|G_i\rangle. \quad (60)$$

Similarly to $|R_i\rangle$, $|R_{i,\phi}\rangle$ possesses only nine non-zero components

$$\begin{aligned} R_{1,\phi} &= F_{x,\phi}, \\ R_{2,\phi} &= F_{y,\phi}, \\ R_{3,\phi} &= F_{z,\phi}, \\ R_{10,\phi} &= F_{y,\phi} c_s^2, \\ R_{11,\phi} &= F_{x,\phi} c_s^2, \\ R_{12,\phi} &= F_{z,\phi} c_s^2, \\ R_{13,\phi} &= F_{x,\phi} c_s^2, \\ R_{14,\phi} &= F_{z,\phi} c_s^2, \\ R_{15,\phi} &= F_{y,\phi} c_s^2. \end{aligned} \quad (61)$$

Post-collision central moments are then corrected with the forcing term [see Eq. (A10)]. Eventually, post-collision populations are given by

$$|g_i^*\rangle = \mathbf{T}^{-1}|k_{i,\phi}^*\rangle. \quad (62)$$

Again, a two-step approach can be adopted, i.e.,

$$|g_i^*\rangle = \mathbf{M}^{-1}\mathbf{N}^{-1}|k_{i,\phi}^*\rangle. \quad (63)$$

As done before, we first compute raw moments as

$$|r_{i,\phi}^*\rangle = \mathbf{N}^{-1}|k_{i,\phi}^*\rangle. \quad (64)$$

The expressions of $|r_{i,\phi}^*\rangle$ can be found in the D3Q19-CentralMoments-PhaseField.m script attached in the [supplementary material](#). Then, post-collision populations can be constructed as

$$|g_i^*\rangle = \mathbf{M}^{-1}|r_{i,\phi}^*\rangle. \quad (65)$$

These are equal to

$$\begin{aligned}
g_0^* &= r_{0,\phi}^* - r_{4,\phi}^* + r_{16,\phi}^* + r_{17,\phi}^* + r_{18,\phi}^*, \\
g_1^* &= (r_{4,\phi}^* + 2r_{5,\phi}^* + r_{6,\phi}^*)c_s^2/2 - (-r_{1,\phi}^* + r_{11,\phi}^* + r_{13,\phi}^* + r_{16,\phi}^* + r_{17,\phi}^*)/2, \\
g_2^* &= (r_{4,\phi}^* + 2r_{5,\phi}^* + r_{6,\phi}^*)c_s^2/2 + (r_{11,\phi}^* + r_{13,\phi}^* - r_{1,\phi}^* - r_{16,\phi}^* - r_{17,\phi}^*)/2, \\
g_3^* &= (r_{4,\phi}^* - r_{5,\phi}^* + r_{6,\phi}^*)c_s^2/2 - (-r_{2,\phi}^* + r_{10,\phi}^* + r_{15,\phi}^* + r_{16,\phi}^* + r_{18,\phi}^*)/2, \\
g_4^* &= (r_{4,\phi}^* - r_{5,\phi}^* + r_{6,\phi}^*)c_s^2/2 - (r_{2,\phi}^* - r_{10,\phi}^* - r_{15,\phi}^* + r_{16,\phi}^* + r_{18,\phi}^*)/2, \\
g_5^* &= (r_{4,\phi}^* - r_{5,\phi}^* - 2r_{6,\phi}^*)c_s^2/2 - (-r_{3,\phi}^* + r_{12,\phi}^* + r_{14,\phi}^* + r_{17,\phi}^* + r_{18,\phi}^*)/2, \\
g_6^* &= (r_{4,\phi}^* - r_{5,\phi}^* - 2r_{6,\phi}^*)c_s^2/2 - (r_{3,\phi}^* - r_{12,\phi}^* - r_{14,\phi}^* + r_{17,\phi}^* + r_{18,\phi}^*)/2, \\
g_7^* &= (r_{7,\phi}^* + r_{10,\phi}^* + r_{11,\phi}^* + r_{16,\phi}^*)/4, \\
g_8^* &= (r_{7,\phi}^* + r_{16,\phi}^* - r_{10,\phi}^* - r_{11,\phi}^*)/4, \\
g_9^* &= (r_{11,\phi}^* + r_{16,\phi}^* - r_{7,\phi}^* - r_{10,\phi}^*)/4, \\
g_{10}^* &= (r_{10,\phi}^* + r_{16,\phi}^* - r_{7,\phi}^* - r_{11,\phi}^*)/4, \\
g_{11}^* &= (r_{8,\phi}^* + r_{12,\phi}^* + r_{13,\phi}^* + r_{17,\phi}^*)/4, \\
g_{12}^* &= (r_{8,\phi}^* + r_{17,\phi}^* - r_{12,\phi}^* - r_{13,\phi}^*)/4, \\
g_{13}^* &= (r_{13,\phi}^* + r_{17,\phi}^* - r_{8,\phi}^* - r_{12,\phi}^*)/4, \\
g_{14}^* &= (r_{12,\phi}^* + r_{17,\phi}^* - r_{8,\phi}^* - r_{13,\phi}^*)/4, \\
g_{15}^* &= (r_{9,\phi}^* + r_{14,\phi}^* + r_{15,\phi}^* + r_{18,\phi}^*)/4, \\
g_{16}^* &= (r_{9,\phi}^* + r_{18,\phi}^* - r_{14,\phi}^* - r_{15,\phi}^*)/4, \\
g_{17}^* &= (r_{15,\phi}^* + r_{18,\phi}^* - r_{9,\phi}^* - r_{14,\phi}^*)/4, \\
g_{18}^* &= (r_{14,\phi}^* + r_{18,\phi}^* - r_{9,\phi}^* - r_{15,\phi}^*)/4.
\end{aligned} \tag{66}$$

Eventually, these are streamed by Eq. (7). It is of interest to note that Eq. (66) look very similar to Eq. (47). Indeed the former can be obtained by substituting r_i^* by $r_{i,\phi}^*$ in the latter. This is due to the fact that the very same lattice structure (the D3Q19 one) and transformation matrices (\mathbf{M} and \mathbf{N}) are adopted for both the sets of populations (f_i and g_i).

The formulation in terms of raw moments can be obtained, again, by setting $\mathbf{N} = \mathbf{I}$. In this case, equilibrium and post-collision RMs are

$$\begin{aligned}
r_{0,\phi}^{eq} &= \phi, \\
r_{1,\phi}^{eq} &= \phi u_x, \\
r_{2,\phi}^{eq} &= \phi u_y, \\
r_{3,\phi}^{eq} &= \phi u_z, \\
r_{4,\phi}^{eq} &= \phi(u_x^2 + u_y^2 + u_z^2 + 1), \\
r_{5,\phi}^{eq} &= \phi(u_x^2 - u_y^2), \\
r_{6,\phi}^{eq} &= \phi(u_y^2 - u_z^2), \\
r_{7,\phi}^{eq} &= \phi u_x u_y, \\
r_{8,\phi}^{eq} &= \phi u_x u_z, \\
r_{9,\phi}^{eq} &= \phi u_y u_z, \\
r_{10,\phi}^{eq} &= \phi u_y(u_x^2 + c_s^2), \\
r_{11,\phi}^{eq} &= \phi u_x(u_y^2 + c_s^2), \\
r_{12,\phi}^{eq} &= \phi u_z(u_x^2 + c_s^2), \\
r_{13,\phi}^{eq} &= \phi u_x(u_z^2 + c_s^2),
\end{aligned}$$

$$\begin{aligned}
r_{14,\phi}^{eq} &= \phi u_z(u_y^2 + c_s^2), \\
r_{15,\phi}^{eq} &= \phi u_y(u_z^2 + c_s^2), \\
r_{16,\phi}^{eq} &= \phi(3u_x^2 + 1)(3u_y^2 + 1)c_s^4, \\
r_{17,\phi}^{eq} &= \phi(3u_x^2 + 1)(3u_z^2 + 1)c_s^4, \\
r_{18,\phi}^{eq} &= \phi(3u_y^2 + 1)(3u_z^2 + 1)c_s^4
\end{aligned} \tag{67}$$

and

$$\begin{aligned}
r_{0,\phi}^* &= \phi, \\
r_{1,\phi}^* &= (1 - \omega_\phi)r_{1,\phi} + \omega_\phi\phi u_x - F_{x,\phi}(\omega_\phi/2 - 1), \\
r_{2,\phi}^* &= (1 - \omega_\phi)r_{2,\phi} + \omega_\phi\phi u_y - F_{y,\phi}(\omega_\phi/2 - 1), \\
r_{3,\phi}^* &= (1 - \omega_\phi)r_{3,\phi} + \omega_\phi\phi u_z - F_{z,\phi}(\omega_\phi/2 - 1), \\
r_{4,\phi}^* &= \phi(u_x^2 + u_y^2 + u_z^2 + 1), \\
r_{5,\phi}^* &= \phi(u_x^2 - u_y^2), \\
r_{6,\phi}^* &= \phi(u_y^2 - u_z^2), \\
r_{7,\phi}^* &= \phi u_x u_y, \\
r_{8,\phi}^* &= \phi u_x u_z, \\
r_{9,\phi}^* &= \phi u_y u_z, \\
r_{10,\phi}^* &= F_{y,\phi}c_s^2/2 + \phi u_y(u_x^2 + c_s^2), \\
r_{11,\phi}^* &= F_{x,\phi}c_s^2/2 + \phi u_x(u_y^2 + c_s^2), \\
r_{12,\phi}^* &= F_{z,\phi}c_s^2/2 + \phi u_z(u_x^2 + c_s^2), \\
r_{13,\phi}^* &= F_{x,\phi}c_s^2/2 + \phi u_x(u_z^2 + c_s^2), \\
r_{14,\phi}^* &= F_{z,\phi}c_s^2/2 + \phi u_z(u_y^2 + c_s^2), \\
r_{15,\phi}^* &= F_{y,\phi}c_s^2/2 + \phi u_y(u_z^2 + c_s^2), \\
r_{16,\phi}^* &= \phi(3u_x^2 + 1)(3u_y^2 + 1)c_s^4, \\
r_{17,\phi}^* &= \phi(3u_x^2 + 1)(3u_z^2 + 1)c_s^4, \\
r_{18,\phi}^* &= \phi(3u_y^2 + 1)(3u_z^2 + 1)c_s^4,
\end{aligned} \tag{68}$$

respectively. Post-collision populations can be computed by Eq. (66) and eventually streamed by Eq. (7).

We conclude this section by highlighting a salient feature of the outlined approach. Following Refs. 41 and 43, the quantity:

$$\mathbf{n} = [n_x, n_y, n_z] = \frac{\nabla\phi}{|\nabla\phi|} \tag{69}$$

in Eq. (16) can be immediately obtained as

$$\begin{aligned}
n_x &= -\frac{k_{1,\phi}}{\sqrt{k_{1,\phi}^2 + k_{2,\phi}^2 + k_{3,\phi}^2 + \epsilon}}, \\
n_y &= -\frac{k_{2,\phi}}{\sqrt{k_{1,\phi}^2 + k_{2,\phi}^2 + k_{3,\phi}^2 + \epsilon}}, \\
n_z &= -\frac{k_{3,\phi}}{\sqrt{k_{1,\phi}^2 + k_{2,\phi}^2 + k_{3,\phi}^2 + \epsilon}}
\end{aligned} \tag{70}$$

without requiring the (possibly time-consuming) computation of spatial derivatives by Eq. (20). The impact of this choice is evaluated in

Sec. III both in terms of accuracy and computational time. $\epsilon = 10^{-12}$ is a very small number added in order to avoid a possible division by zero.

III. NUMERICAL TESTS

In this section, we discuss the results of our numerical campaign. Tests are divided into two groups. The former is composed of the following cases:

- diagonal translation of a circular interface;
- Zalesak disk;
- circular interface in a shear flow;
- deformation of a circular interface in a smoothed shear flow;
- deformation of a spherical interface in a smoothed shear flow;
- swirling deformation of a spherical interface.

These tests are used to evaluate the ability of the algorithm to capture the correct evolution of the interface. The velocity field is superimposed in advance; hence, only the evolution of the order parameter needs to be solved. This velocity field aims at distorting and deforming the interface, which should return in its initial configuration at the end of each run. The accuracy of the method is quantitatively evaluated by computing the L2-norm of the relative error between the order parameter at the end of the simulation and the initial (expected) one, that is,

$$\varepsilon = \sqrt{\frac{\sum_x [\phi(\mathbf{x}, t) - \phi(\mathbf{x}, t=0)]^2}{\sum_x [\phi(\mathbf{x}, t=0)]^2}}. \quad (71)$$

Presents findings are compared to those obtained by other LB efforts.^{40,41,43,45,48,52} The computation of the gradient of ϕ is performed by using finite differences [FD, see Eq. (20)] and moments [Mom, see Eq. (70)]. Unless otherwise stated, we adopt $M = 0.001$, $\xi = 3$ and $U_0 = 0.02$, which corresponds to a Mach number equal to $\text{Ma} = \frac{U_0}{c_s} \approx 0.035$. This value can be considered sufficiently low to annihilate deleterious compressibility effects affecting the solution of the LBEs. Runs are characterized by a reference time defined as $T = L_0/U_0$. Periodic boundary conditions are enforced at each side of the domain within this group of simulations.

In the latter group, two immiscible fluids are considered and the evolutions of both the velocity and order parameter are evaluated. The following scenarios are investigated:

- vertical penetration of a wedge-shaped body;
- two-dimensional Rayleigh–Taylor instability^{42,55,65} at $\text{Re} = 256$, $\text{At} = 0.5$, $\text{Ca} = 0.26$ and $\text{Pe} = 500$;
- $\text{Re} = 3000$, $\text{At} = 0.5$, $\text{Ca} = 0.26$ and $\text{Pe} = 1000$;
- $\text{Re} = 30\,000$, $\text{At} = 0.5$, $\text{Ca} = 0.26$ and $\text{Pe} = 500$;
- three-dimensional Rayleigh–Taylor instability at $\text{Re} = 256$, $\text{At} = 0.5$, $\text{Ca} = 960$ and $\text{Pe} = 1024$.

Notice that the Atwood number is defined $\text{At} = (\rho_H - \rho_L)/(\rho_H + \rho_L)$ and the capillarity number is $\text{Ca} = \mu_H U_0/\sigma$.

Unless otherwise stated, all the illustrations report findings obtained by using finite differences to estimate $\nabla\phi$. Moreover, when a two-dimensional case is considered, this is achieved by using only one lattice points in the direction z and u_z is set equal to zero.

A. Diagonal translation of a circular interface

Let us consider a circular interface of radius $R = L_0/5$ located at the center of a domain of size $L_0 \times L_0$ with $L_0 = 200$. The order parameter is initialized as

$$\phi(\mathbf{x}, t=0) = \frac{\phi_H + \phi_L}{2} + \frac{\phi_H - \phi_L}{2} \tanh\left(2 \frac{R - |\mathbf{x} - \mathbf{x}_0|}{\xi}\right), \quad (72)$$

where $\mathbf{x}_0 = (100, 100)$ is the location of the center of the circular interface. A constant uniform velocity field $\mathbf{u} = (U_0, U_0)$ is superimposed.⁵² Simulations are carried out until $t = 10T$ when the interface is expected to occupy the same position as the one prescribed at the beginning of the simulation. The error achieved by the present method is reported in Table I and is compared to the one obtained by other LB efforts. Independently from the methodology adopted to compute the gradient of the order parameter (FD or Mom), the proposed approach outperforms the schemes devised in Refs. 41 and 48 in terms of accuracy. Moreover, our solution goes closer to the one in Ref. 52 for the highest value of the Peclet number.

Furthermore, let us discuss a scenario where the Peclet number is increased to 8000. Figure 1 sketches the interface obtained by our approach after ten cycles. The adoption of moments induces some ripples at the interface. Conversely, FD gives us a smoother surface. This behavior corroborates findings in Ref. 41 and should be addressed to the presence of grid-scale oscillations affecting the former.

This test is repeated by adopting the setup in Ref. 41 where $L_0 = 100$ and $R = L_0/4$. It should be noted that Ref. 41 defines the Peclet number as $\text{Pe} = \frac{U_0 \xi}{M} = 60$ and we match this value in our simulations. The good accuracy properties of our methodology are confirmed in Table II, where findings are more accurate than those obtained by Refs. 40 and 45 and the moment-based approach in Ref. 41. Conversely, the adoption of finite differences in Ref. 41 shows a considerable advantage.

B. Zalesak disk

A slotted circular disk of radius $R = 80$ is initially located at the center of a domain of size $L_0 \times L_0$ with $L_0 = 200$.⁸¹ The width of the slot is equal to 15. The rotation of the disk is driven by a constant velocity field

TABLE I. Diagonal translation of a circular interface: relative error at different Pe. Setup as in Ref. 52. Reproduced by Zu *et al.*, “Phase-field lattice Boltzmann model for interface tracking of a binary fluid system based on the Allen–Cahn equation,” with permission from Phys. Rev. E **102**, 053307 (2020). Copyright 2020 APS Publishing.

Model	Pe		
	125	500	2000
FD	0.0066	0.0050	0.0090
Mom	0.0121	0.0303	0.0588
Ref. 52 (Zu <i>et al.</i>)	0.0032	0.0021	0.0084
Ref. 52 (Geier <i>et al.</i>)	0.0363	0.0107	0.0600
Ref. 52 (Wang <i>et al.</i>)	0.0359	0.0106	0.0596

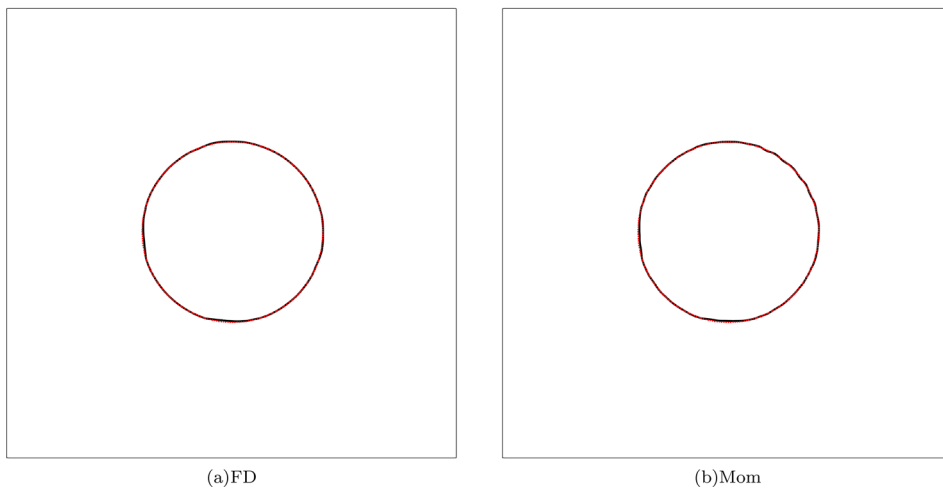


FIG. 1. Diagonal translation of a circular interface: interface (solid black line) at $t = 10T$ when $\text{Pe} = 8000$ by using (a) FD and (b) Mom. The initial shape (red dotted line) is superimposed for comparison.

TABLE II. Diagonal translation of a circular interface: relative error at different Pe. Setup as in Ref. 41. Reproduced with permission from Geier *et al.* “Conservative phase-field lattice Boltzmann model for interface tracking equation,” Phys. Rev. E **91**, 063309 (2015). Copyright 2015 APS Publishing.

Model	ε
FD	0.0134
Mom	0.0458
Ref. 41 (Zu and He)	0.1176
Ref. 41 FD	0.0074
Ref. 41 Mom	0.0874

$$\begin{aligned} u_x &= -U_0 2\pi \left(\frac{y}{L_0} - 0.5 \right), \\ u_y &= U_0 2\pi \left(\frac{x}{L_0} - 0.5 \right). \end{aligned} \quad (73)$$

The disk is supposed to return to the initial position after a period T . **Table III** reports the relative error with respect to the initial configuration for different values of the Peclet numbers. One can immediately observe the superior accuracy properties of the proposed scheme

TABLE III. Zalesak disk: relative error at different Pe. Reproduced by Zu *et al.*, “Phase-field lattice Boltzmann model for interface tracking of a binary fluid system based on the Allen-Cahn equation,” with permission from Phys. Rev. E **102**, 053307 (2020). Copyright 2020 APS Publishing

Model	Pe			
	80	400	800	4000
FD	0.0593	0.0590	0.0558	0.0505
Mom	0.0567	0.0482	0.0483	0.0501
Ref. 52 (Zu <i>et al.</i>)	0.1226	0.1186	0.1170	0.1194
Ref. 52 (Geier <i>et al.</i>)	0.1307	0.1224	0.1209	0.1472
Ref. 52 (Wang <i>et al.</i>)	0.1307	0.1224	0.1209	0.1471

independently from the value of Pe and from the strategy employed to compute $\nabla\phi$. Notably, the error is at least reduced by a half with respect to the one obtained by other LB efforts. [Figure 2](#) depicts the interface at salient time instants. Very small ripples are experienced at its tips independently from the adoption of finite differences or moments.

This test case is further adopted to estimate the computational cost in terms of involved central processing unit (CPU) time. Specifically, we measure the run time of the algorithm adopting finite difference, as well as the one with moments, by varying the number of lattice sites as $L_0 = 100, 200, 300, 400$. All the values of the CPU time are then normalized by the fastest run, that is, the one corresponding to $L_0 = 100$ when moments are adopted. We report in [Fig. 3](#) the normalized CPU time against L_0 . It is possible to observe that employing moments to compute the gradient of the order parameter clearly reduces the computational cost. This improvement becomes more emphasized as the number of lattice points grows. This trend should be addressed to the fact that the Mom strategy is a purely local approach.

C. Circular interface in a shear flow

Let us consider a square domain of size $L_0 \times L_0$ with $L_0 = 200$. A circular interface of radius $R = L_0/5$ is placed at $x_0 = (100, 60)$. The domain undergoes a shear velocity field defined as^{41,82}

$$\begin{aligned} u_x &= -U_0 \pi \cos \left[\pi \left(\frac{x}{L_0} - 0.5 \right) \right] \sin \left[\pi \left(\frac{y}{L_0} - 0.5 \right) \right], \\ u_y &= U_0 \pi \cos \left[\pi \left(\frac{x}{L_0} - 0.5 \right) \right] \sin \left[\pi \left(\frac{y}{L_0} - 0.5 \right) \right]. \end{aligned} \quad (74)$$

At $t = T$, this field is reversed (i.e., the two components of the velocity are multiplied by a factor equal to -1). The interface is expected to come back to its original position at $t = 2T$. Making reference at [Fig. 4](#), the maximum stretch is achieved at $t = T$, where the interface shows a prominent elongated tail. This corroborates findings in Ref. 41, where the very same pattern is observed. Notice that the simulation corresponding to the adoption of moments to compute $\nabla\phi$ produces a slightly more jagged final surface due to the aforementioned grid-scale oscillations. A more quantitative estimation of the relative error reported in [Table IV](#) attests the very good accuracy of the method.

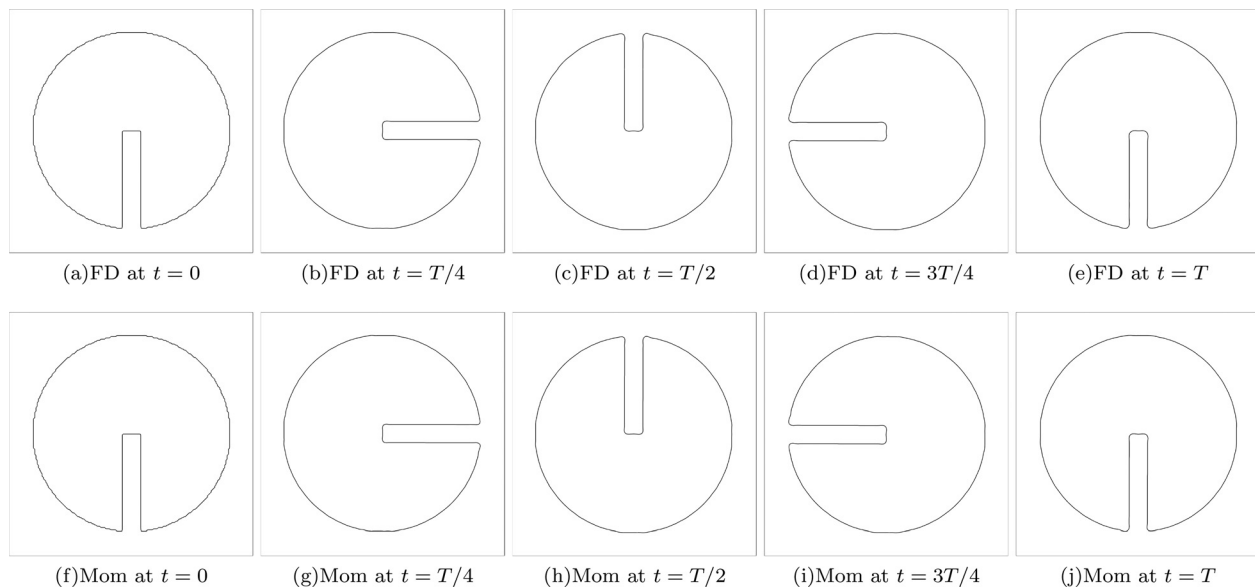


FIG. 2. Zalesak disk at $\text{Pe} = 4000$: interface obtained by finite differences at (a) $t = 0$, (b) $t = T/4$, (c) $t = T/2$, (d) $t = 3T/4$, (e) $t = T$ and moments at (f) $t = 0$, (g) $t = T/4$, (h) $t = T/2$, (i) $t = 3T/4$, (j) $t = T$.

D. Deformation of a circular interface in a smoothed shear flow

We now consider a stringent benchmark case where the interface undergoes large topological changes and severe deformations.^{40,41,45,48,52} Let us consider a square domain of size $L_0 \times L_0$ with $L_0 = 512$. A circular interface of radius $R = L_0/5$ placed in the center of the domain is subject to a smoothed time-dependent and strongly non-linear flow field defined as

$$\begin{aligned} u_x &= -U_0 \sin\left(4\pi \frac{x}{L_0}\right) \sin\left(4\pi \frac{y}{L_0}\right) \cos\left(\pi \frac{t}{T}\right), \\ u_x &= -U_0 \cos\left(4\pi \frac{x}{L_0}\right) \cos\left(4\pi \frac{y}{L_0}\right) \cos\left(\pi \frac{t}{T}\right). \end{aligned} \quad (75)$$

Simulations are carried out by setting the Cahn number equal to 1/256. As shown in Table V, the error achieved by the present strategy is comparable to the one obtained by other LB efforts. As shown in Fig. 5, the interface undergoes a symmetric transfiguration-reconstruction process. The largest topological change of the interface takes place at $t = T/2$, when a particularly thin filamentary structure is recognizable in the middle of the domain along the vertical axis of symmetry. These observations confirm findings achieved by other authors.^{40,41,45,48,52}

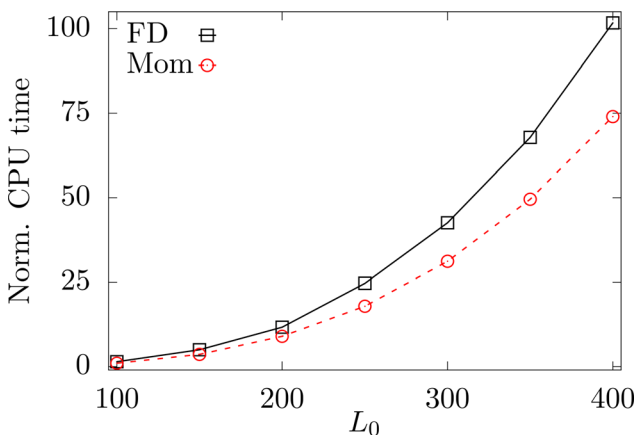


FIG. 3. Zalesak disk: requested CPU time against the number of lattice points L_0 by adopting finite differences (FD, black solid line with squares) and moments (Mom, red dashed line with circles) to compute the gradient of the order parameter. CPU time is normalized by the fastest run, that is, the one corresponding to $L_0 = 100$ when moments are employed.

E. Spherical interface in a shear flow

Let us consider a sphere of radius $R = L_0/5$ located at $\mathbf{x}_0 = (3L_0/10, 3L_0/10, L_0/2)$ in a cubic domain $L_0 \times L_0 \times L_0$ with $L_0 = 100$.⁵² The superimposed velocity field is

$$\begin{aligned} u_x &= U_0 \pi \cos\left[\pi\left(\frac{x}{L_0} - 0.5\right)\right] \left\{ \sin\left[\pi\left(\frac{z}{L_0} - 0.5\right)\right] \right. \\ &\quad \left. - \sin\left[\pi\left(\frac{y}{L_0} - 0.5\right)\right]\right\} \cos\left(2\pi \frac{t}{T}\right), \end{aligned} \quad (76)$$

$$\begin{aligned} u_y &= U_0 \pi \cos\left[\pi\left(\frac{y}{L_0} - 0.5\right)\right] \left\{ \sin\left[\pi\left(\frac{x}{L_0} - 0.5\right)\right] \right. \\ &\quad \left. - \sin\left[\pi\left(\frac{z}{L_0} - 0.5\right)\right]\right\} \cos\left(2\pi \frac{t}{T}\right), \end{aligned} \quad (77)$$

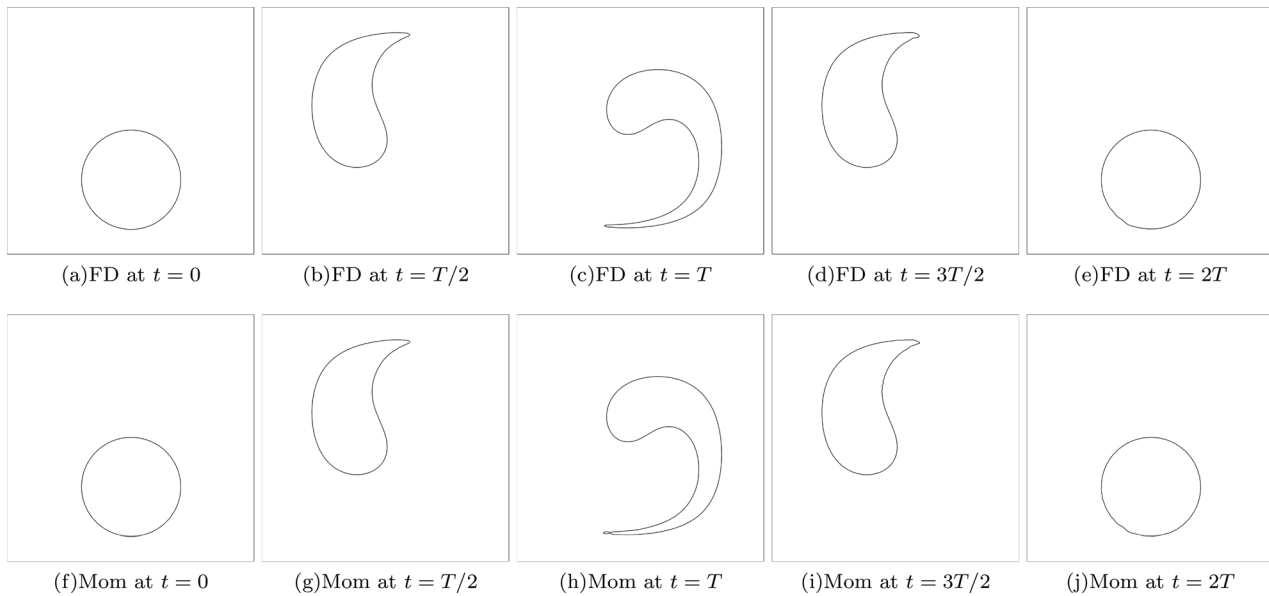


FIG. 4. Circular interface in a shear flow: interface obtained by finite differences at (a) $t = 0$, (b) $t = T/2$, (c) $t = T$, (d) $t = 3T/2$, (e) $t = 2T$ and moments at (f) $t = 0$, (g) $t = T/2$, (h) $t = T$, (i) $t = 3T/2$, (j) $t = 2T$.

TABLE IV. Circular interface in a shear flow: relative error. Reproduced with permission from Geier *et al.* “Conservative phase-field lattice Boltzmann model for interface tracking equation,” Phys. Rev. E **91**, 063309 (2015). Copyright 2015 APS Publishing.

Model	ε
FD	0.0244
Mom	0.0270
Ref. 41 (Zu and He)	0.0403
Ref. 41 FD	0.0216
Ref. 41 Mom	0.0274

$$u_z = U_0 \pi \cos \left[\pi \left(\frac{z}{L_0} - 0.5 \right) \right] \left\{ \sin \left[\pi \left(\frac{y}{L_0} - 0.5 \right) \right] - \sin \left[\pi \left(\frac{x}{L_0} - 0.5 \right) \right] \right\} \cos \left(2\pi \frac{t}{T} \right). \quad (78)$$

TABLE V. Deformation of a circular interface in a smoothed shear flow: relative error. Reproduced by Zu *et al.*, “Phase-field lattice Boltzmann model for interface tracking of a binary fluid system based on the Allen-Cahn equation,” with permission from Phys. Rev. E **102**, 053307 (2020). Copyright 2020 APS Publishing

Model	ε
FD	0.0199
Mom	0.0204
Ref. 52 (Zu <i>et al.</i>)	0.0125
Ref. 52 (Geier <i>et al.</i>)	0.0136
Ref. 52 (Wang <i>et al.</i>)	0.0139

Figure 6 demonstrates that the large topological changes of the interface can be successfully captured.⁵² The adoption of moments to compute the gradient of the order parameter leads to a less smooth final shape of the sphere (see Fig. 7), thus corroborating the behavior observed in two-dimensional scenarios.

Let us compare the performance of the present methodology to the one of the D3Q7 model devised by Fakhari *et al.*,⁴³ where moments are employed to compute $\nabla\phi$. Table VI reported the relative error with respect to the initial configuration obtained by the two LBMs. The present D3Q19 approach shows the best performance, thus confirming that increasing the lattice direction enhances the accuracy of the results. However, spanning nineteen directions instead of seven unavoidably increases the computational cost of the run.

F. Swirling deformation of a spherical interface

The last test involving the sole interface tracking method forces a sphere of radius $R = L_0/5$ with center at $x_0 = (L_0/2, L_0/2, L_0/2)$ to undergo more prominent stretching and deformation. The following velocity field is imposed:^{43,83}

$$\begin{aligned} u_x &= \frac{U_0}{2} [\sin(4\pi(x/L_0 - 0.5)) \sin(4\pi(y/L_0 - 0.5)) \\ &\quad + \cos(4\pi(z/L_0 - 0.5)) \cos(4\pi(x/L_0 - 0.5))] \cos(\pi t), \\ u_y &= \frac{U_0}{2} [\sin(4\pi(y/L_0 - 0.5)) \sin(4\pi(z/L_0 - 0.5)) \\ &\quad + \cos(4\pi(x/L_0 - 0.5)) \cos(4\pi(y/L_0 - 0.5))] \cos(\pi t), \\ u_z &= \frac{U_0}{2} [\sin(4\pi(z/L_0 - 0.5)) \sin(4\pi(x/L_0 - 0.5)) \\ &\quad + \cos(4\pi(y/L_0 - 0.5)) \cos(4\pi(z/L_0 - 0.5))] \cos(\pi t). \end{aligned} \quad (79)$$

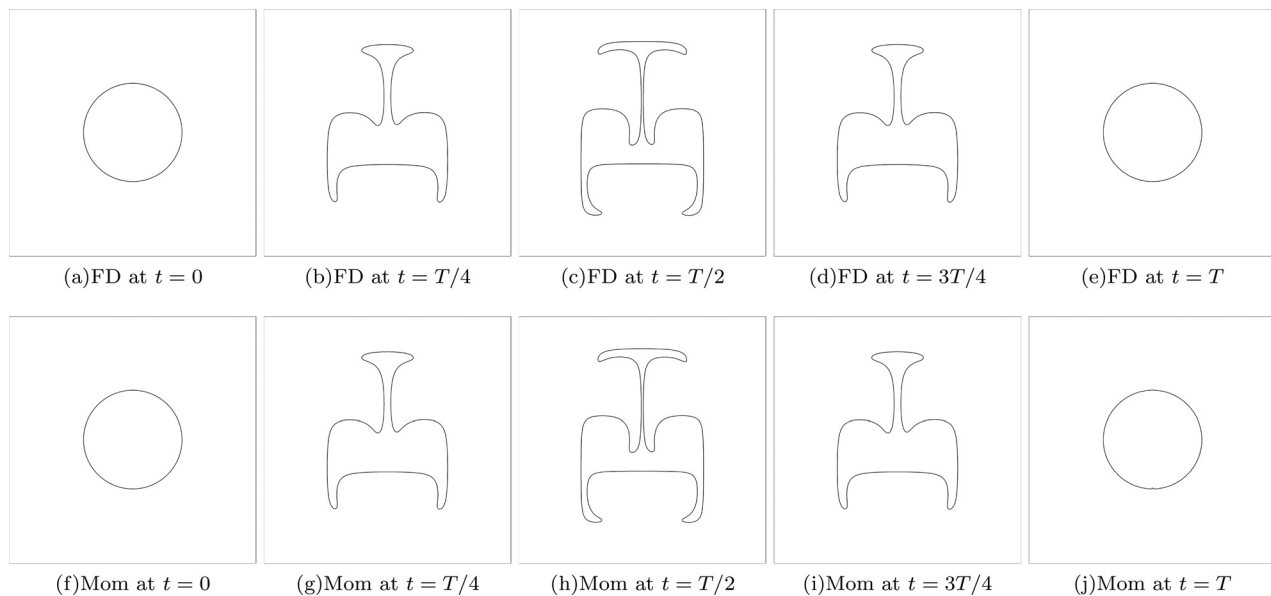


FIG. 5. Deformation of a circular interface in a smoothed shear flow: interface obtained by finite differences at (a) $t = 0$, (b) $t = T/4$, (c) $t = T/2$, (d) $t = 3T/4$, (e) $t = T$ and moments at (f) $t = 0$, (g) $t = T/4$, (h) $t = T/2$, (i) $t = 3T/4$, (j) $t = T$.

The simulation run until $t = T$, when the interface is supposed to restore its initial shape. The severe deformation can be appreciated in Fig. 8, where the interface is sketched at $t = 3T/4$ by adopting the present scheme and the D3Q7 LBM in Ref. 43. In both cases, moments are adopted to compute $\nabla\phi$. Both the approaches produce some wrinkles on the interface, which are alleviated when nineteen speeds are adopted. We expect that these will be further damped by adopting finer grid resolutions. Similarly to the previous case, Table VII confirms that the adoption of more lattice directions increases the accuracy of the numerical run.

G. Vertical penetration of a wedge

Let us consider a system composed of two immiscible fluids: the heavy one, water, with $\rho_H = 1000 \text{ kg/m}^3$ and $\nu_H = 10^{-6} \text{ m}^2/\text{s}$; the light one, air, with $\rho_L = 1.225 \text{ kg/m}^3$ and $\nu_L = 1.5 \times 10^{-5} \text{ m}^2/\text{s}$. Let us consider a symmetric wedge-shaped body with deadrise angle ζ impacting a quiescent water-free surface at a constant uniform downward velocity equal to $v = 1 \text{ m/s}$. The length of the semi-wedge is $D = 1 \text{ m}$. The moving wedge is accounted for by the Immersed Boundary method.^{84–87} In short, the wedge is represented by a set of nodes that can freely move on the underlying lattice grid. A body force term is generated and accounted for in \mathbf{F}_b [see Eq. (22)].⁸⁸ By assuming the fluid to be inviscid and the flow to be incompressible and irrotational, Wagner⁸⁹ solved analytically the problem within the potential flow theory. Specifically, he proposed that the force experienced by the semi-wedge can be written as

$$F_W(t) = \rho_H \frac{\pi^2 v^2 a(t)}{4 \tan \zeta}, \quad (80)$$

where $a(t) = \pi v t / (2 \tan \zeta)$ is Wagner's wetted length. In a recent paper, De Rosis and Tafuni⁶⁴ computed the pressure resultant by a

D2Q9 phase-field LB model where the gradient of the order parameter was evaluated by finite differences. Here, we repeat this test by adopting the present D3Q19 LBM. Moreover, the role of modifying the estimation of $\nabla\phi$ is investigated. Two different values of the deadrise angle are considered: $\zeta = 2^\circ$ and 3° . The semi-wedge is represented by 500 grid points. 2000 and 1000 lattice points are employed in the horizontal and vertical directions, respectively. Outflow boundary conditions are adopted at each side. The resultant of the pressures acting upon the semi-wedge, P , is computed and compared to the analytical predictions in Ref. 89 and to Smoothed Particle Hydrodynamics (SPH) findings in Ref. 64. Figure 9 depicts the time evolution of these quantities. We experience (i) a linear dependence of P on t and (ii) that forces decrease as the deadrise angle ζ increases. These observations are totally consistent with analytical predictions in Eq. (80). Moreover, the numerical solutions tend to get closer to Wagner's solution for the smaller values of the deadrise angle. This trend is corroborated by the fact that Eq. (80) is valid for vanishing values of ζ . We also find a very good agreement between the pressure resultant obtained by the present approach and then one computed by SPH simulations.⁶⁴

Further insights in the flow physics are given in Fig. 10, where the pressure field is plotted at representative time instants when $\zeta = 3^\circ$. In agreement with findings in Ref. 90, the pressure is maximized in the proximity of the free surface wetting the impacting wedge. Consistently to Wagner's theory,⁸⁹ the pressure attains its minimum at the vertex and this field propagates into the fluid domain by describing semicircular waves.

H. Two-dimensional Rayleigh-Taylor instability

The Rayleigh-Taylor instability is a very popular benchmark to test the ability of a numerical scheme to tackle a system composed of two immiscible fluids.^{91,92} Let us consider a rectangular domain of size

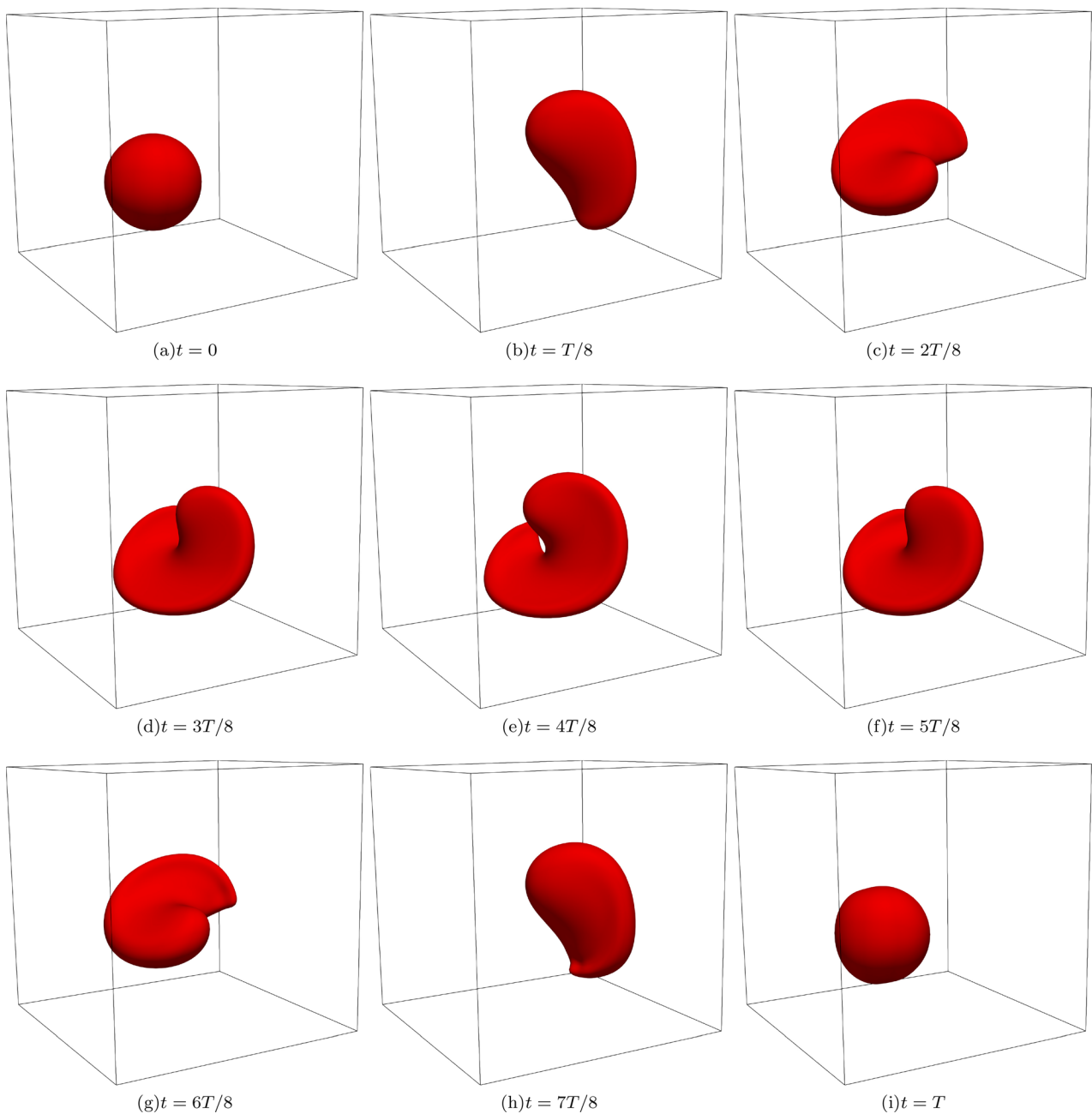


FIG. 6. Spherical interface in a shear flow: interface obtained by finite differences at (a) $t = 0$, (b) $t = T/8$, (c) $t = 2T/8$, (d) $t = 3T/8$, (e) $t = 4T/8$, (f) $t = 5T/8$, (g) $t = 6T/8$, (h) $t = 7T/8$, (i) $t = T$.

$W \times 4W$ with $W = 256$. A heavy fluid is placed on top of a lighter fluid. The velocity is initially set to zero and the order parameter is initialized as

$$\begin{aligned}\phi(\mathbf{x}, t=0) &= \phi_H, \text{ if } y > 2W + 0.1W \cos\left(2\pi \frac{x}{W}\right), \\ \phi(\mathbf{x}, t=0) &= \phi_L, \text{ otherwise.}\end{aligned}\quad (81)$$

No-slip walls are enforced at the top and bottom sections, while the domain is periodic in the horizontal direction. The flow is driven by a gravitational force defined as

$$\mathbf{F} = \left[\rho(\mathbf{x}, t) - \frac{\rho_H + \rho_L}{2} \right] \mathbf{g} \quad (82)$$

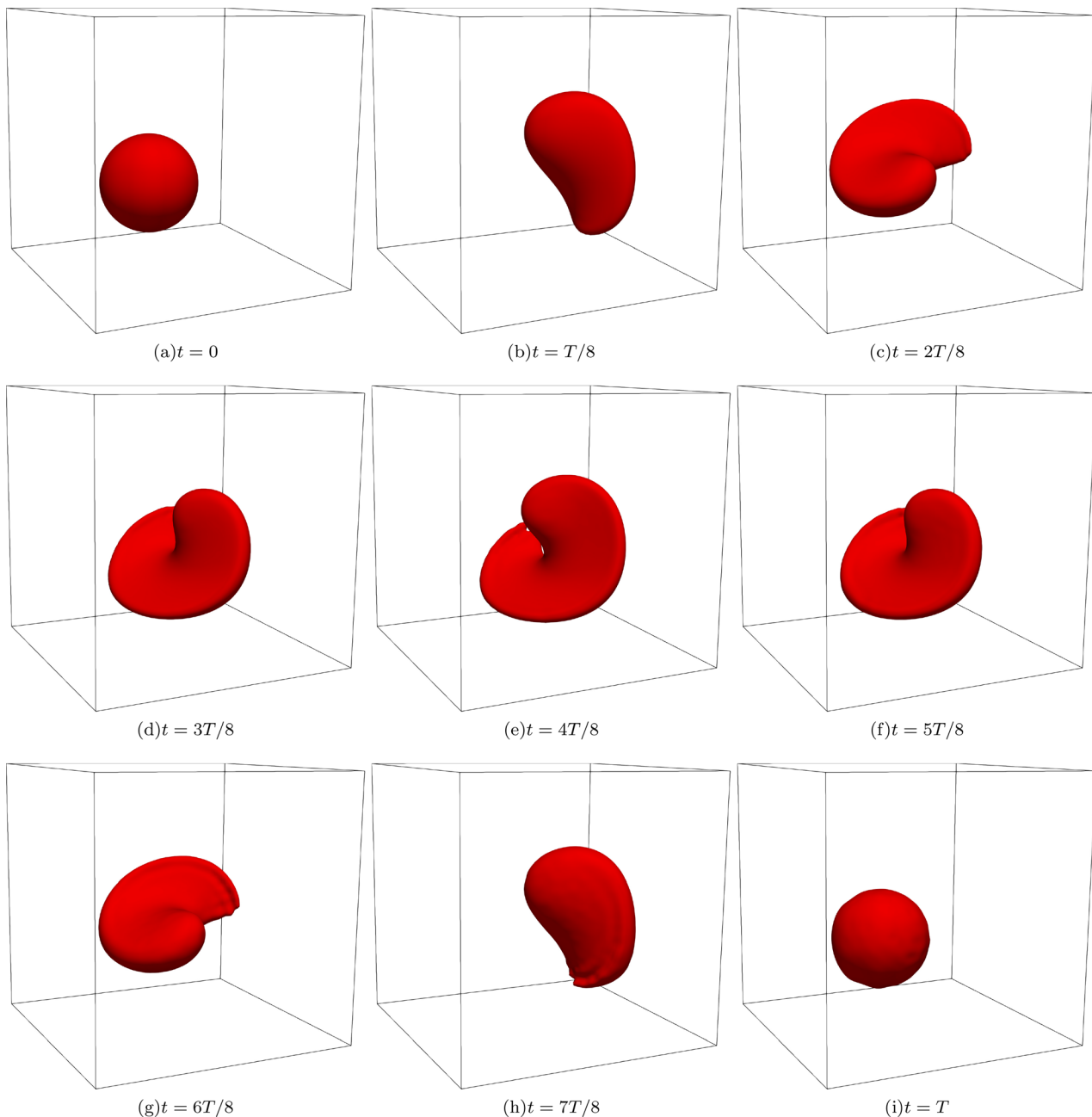


FIG. 7. Spherical interface in a shear flow: interface obtained by moments at (a) $t = 0$, (b) $t = T/8$, (c) $t = 2T/8$, (d) $t = 3T/8$, (e) $t = 4T/8$, (f) $t = 5T/8$, (g) $t = 6T/8$, (h) $t = 7T/8$, (i) $t = 8T/8$.

TABLE VI. Spherical interface in a shear flow: relative error obtained by the D3Q7 LBM and the present D3Q19 LBM.

Model	ε
D3Q7	0.0754
Present	0.0490

with $\mathbf{g} = (0, -g, 0)$. g is chosen so that $\sqrt{gW} = 0.04$.²⁷ The problem is governed by two dimensionless parameters: the Reynolds number $\text{Re} = W\sqrt{gW}/\nu$ and Atwood number $A_t = (\rho_H - \rho_L)/(\rho_H + \rho_L) = 0.5$ (with $\rho_L = 1$). The reference time of the problem is $t_0 = \sqrt{W}/(gA_t)$.

We validate our scheme against the results presented in Refs. 42, 50, 65, and 93 at $\text{Re} = 256$ and 3000. Figure 11 sketches the time

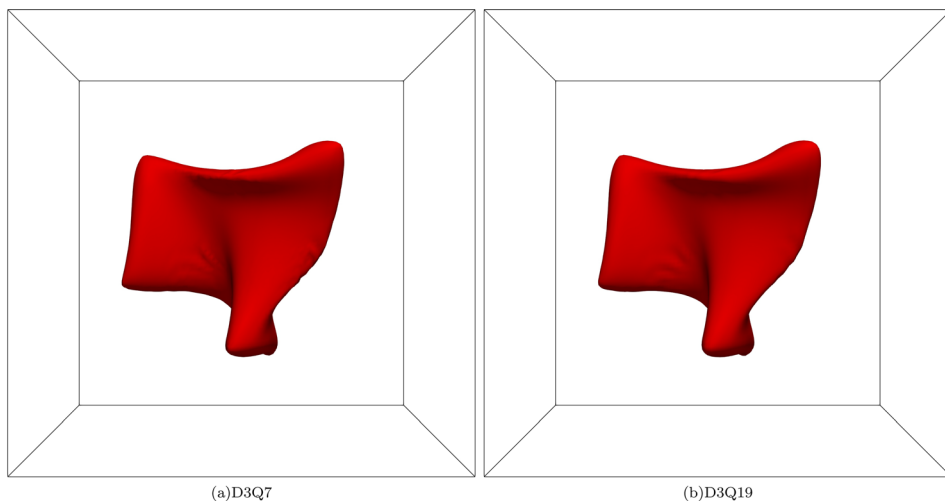


FIG. 8. Deformation of spherical interface: interface at $t = 3T/4$ by (a) D3Q7 LBM and (b) D3Q19 LBM.

TABLE VII. Swirling deformation of spherical interface: relative error obtained by the D3Q7 LBM and the present D3Q19 LBM.

Model	ε
D3Q7	0.1726
Present	0.1133

evolution of the position of the spike of the interface normalized by the width of the domain W , i.e., $y^\dagger = y/W$. One can immediately see that a very good agreement is found between our results and reference ones.

Figures 12 and 13 depict the order parameter at salient time instants when $Re = 256$ and $Re = 3000$, respectively. We experience the downward penetration of the heavy fluid, accompanied by the roll-up of the primary spike and the subsequent generation of the secondary spike in the upward direction. As Re grows, the

breakup of the secondary spike into multiple droplets becomes more prominent. These features corroborate the observations in Fakhari *et al.*,⁴² Dinesh Kumar *et al.*,⁶⁵ and Hosseini *et al.*,⁵⁵ where the very same patterns have been observed. An additional simulation is carried out at $Re = 30\,000$ and the order parameter is reported in Fig. 14. At $t/t_0 = 1$, several Kelvin–Helmholtz instabilities arise along the initial perturbation. Moreover, the presence of smaller-scale structures in the domain appears even more evident. For the sake of reference and completeness, the vertical position of the spike of the interface y^\dagger at $Re = 30\,000$ is reported in Table VIII at representative time instants.

I. Three-dimensional Rayleigh–Taylor instability

We conclude our numerical campaign with the simulation of the three-dimensional Rayleigh–Taylor instability.⁹⁴ A three-dimensional domain of size $W \times 4W \times W$ with $W = 64$ is considered. The order parameter is initialized as

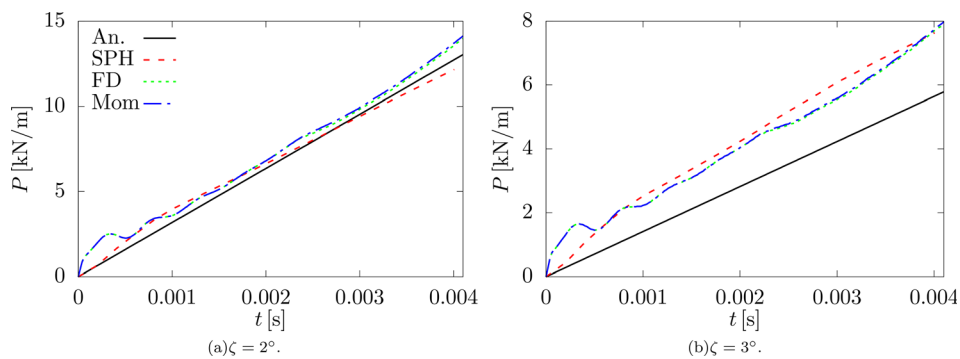


FIG. 9. Vertical penetration of a wedge: time evolution of the pressure force acting upon the semi-wedge computed by Wagner's equation (An., black solid line), SPH simulations in Ref. 64 (red dashed line), present approach by finite differences (FD, green dotted line) and present approach by moments (blue dash-dotted line) at (a) $\zeta = 2^\circ$ and (b) $\zeta = 3^\circ$. Reproduced with permission from A. De Rosis and A. Tafuni, "A phase-field lattice Boltzmann method for the solution of water-entry and water-exit problems," Comput.-Aided Civ. Infrastruct. Eng. (published online 2020). Copyright 2020 John Wiley and Son.

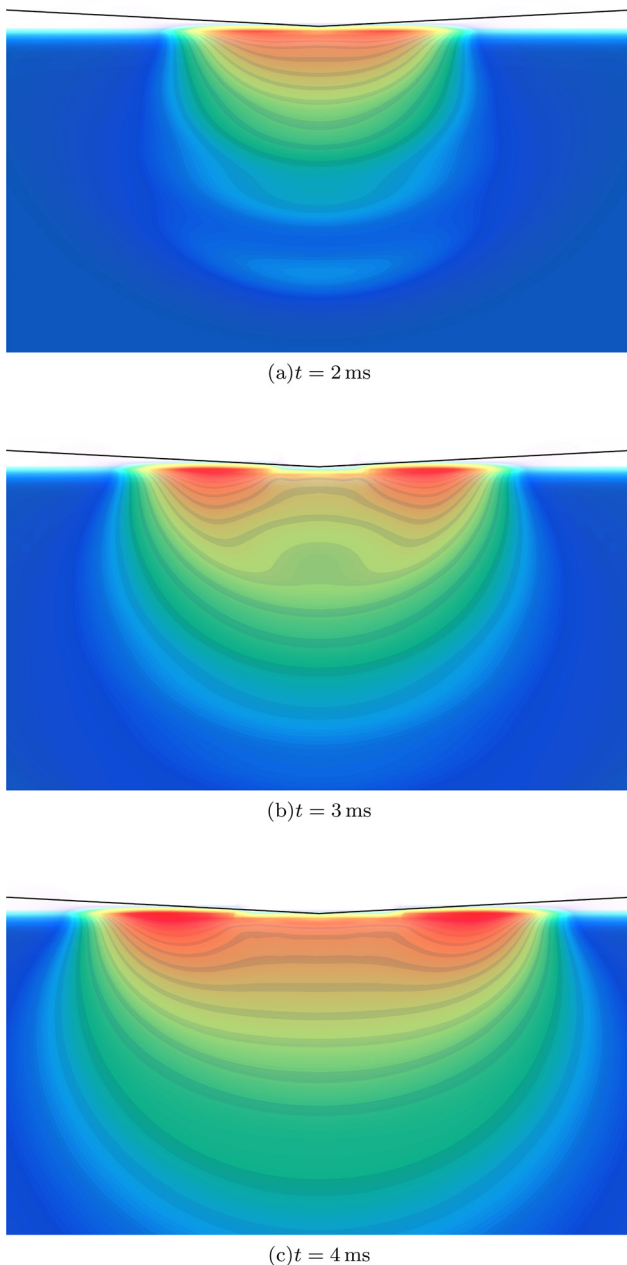


FIG. 10. Vertical penetration of a wedge: contour of the pressure field at (a) $t = 2 \text{ ms}$, (b) $t = 3 \text{ ms}$ and (c) $t = 4 \text{ ms}$. $\zeta = 3^\circ$ is considered. The wedge is represented by a black solid line.

$$\begin{aligned} \phi(\mathbf{x}, t=0) &= \phi_H, \text{ if } y > 2W + 0.05W[\cos(2\pi x) + \cos(2\pi z)], \\ &\phi(\mathbf{x}, t=0) = \phi_L, \text{ otherwise.} \end{aligned} \quad (83)$$

Dimensionless governing parameters are $\text{Re} = 256$, $\text{At} = 0.5$, $\text{Ca} = 960$ and $\text{Pe} = 1024$. Figure 15, the evolution of the interface between the two fluids is sketched at salient time instants. As expected, the

heavy and light fluids penetrate into each other as time increases. The light fluid rises to form a bubble and the heavy fluid falls to generate a mushroom-shaped spike. Four saddle points at the middle of the four sides of the computational box are visible. The interface remains rather simple during the early stage, while becoming more complicated as time increases. At $t/t_0 = 2$, the first roll-up of the heavy fluid appears close to the saddle points due to the presence of a Kelvin-Helmholtz instability mechanism. The roll-up at the edge of the spike starts at a later time. These observations are consistent with consolidated reference data in Ref. 94. A more quantitative analysis of the results is reported in Table IX. The accuracy of the present approach is assessed by comparing the vertical position of the spike at representative time instants to findings obtained by other models:

- the D3Q19-CGM-CM-LBM,⁷⁴ that is a color-gradient LBM with collision operator in terms of central moments in the D3Q19 space;
- the D3Q27-CGM-CM-LBM,⁶² that is a color-gradient LBM with collision operator in terms of central moments in the D3Q27 space;
- the D3Q27-CGM-MRT-LBM,²⁸ that is a color-gradient LBM with collision operator in terms of raw moments in the D3Q27 space;
- the seminal work in Ref. 94, where a D3Q15-BGK LB model for multiphase flows is adopted;
- the D3Q19-phase-field-MRT LB scheme,⁹⁵ that is a phase-field LBM with collision operator in terms of raw moments in the D3Q19 space;
- a solution of the coupled Cahn-Hilliard–Navier–Stokes equations.⁹⁶

The proposed approach shows a satisfying agreement with data from the literature, even though some discrepancies are also observed as the time advances. These could be related to the equilibration of high-order moments as well as the increased bulk viscosity of CMs-based algorithms.^{62,74}

Eventually, we illustrate a turbulent scenario where the Reynolds is set to 3000. Figure 16 shows the presence of many small-scale structures arising as a consequence of Kelvin-Helmholtz instabilities. The roll-up of spike and bubbles is more evident. The heavy fluid falls more rapidly due to the lower viscous friction. The interface impacts the bottom sections at $t/t_0 \sim 3$ after having assumed a more conic shape with respect to the previous case. For the sake of reference, the vertical position of the spike normalized by the width of the domain is reported in Table X for this case.

IV. CONCLUSIONS

We presented a three-dimensional lattice Boltzmann scheme to compute the evolution of a system composed of two fluids by means of the D3Q19 discretization. The two collision processes are written within a general multiple-relaxation-time framework. The proposed approach shows very good accuracy properties, which are evaluated against nine different tests. The performance is particularly satisfying if compared to the adoption of the D3Q7 LBM. The gradient of the order parameter can be computed by finite difference or first-order

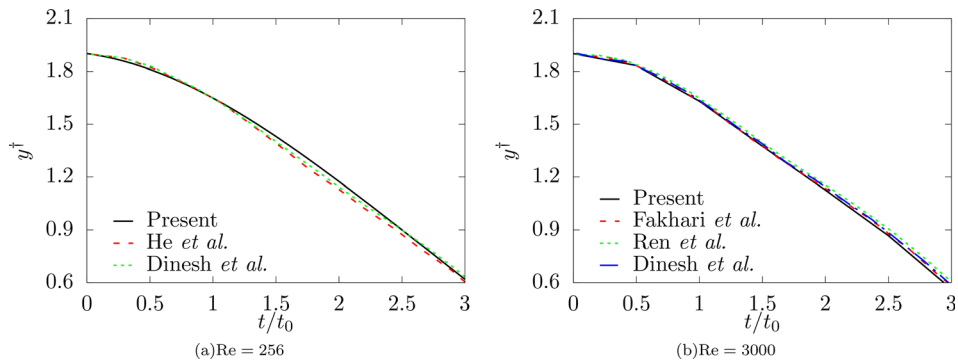


FIG. 11. Two-dimensional Rayleigh–Taylor instability at (a) $Re = 256$ (b) $Re = 3000$. Present findings are compared to those reported by He et al.,⁹³ Dinesh Kumar et al.,⁶⁵ Ren et al.,⁵⁰ and Fakhari et al.⁴² Reproduced with permission from Dinesh Kumar et al., “Phase field lattice Boltzmann model for air–water two phase flows,” Phys. Fluids 31, 072103 (2019). Copyright 2019 AIP Publishing. Reproduced with permission from He et al., “A lattice Boltzmann scheme for incompressible multiphase flow and its application in simulation of Rayleigh–Taylor instability,” J. Comput. Phys. 152, 642–663 (1999). Copyright 1999 Elsevier. Reproduced with permission from Ren et al., “Improved lattice Boltzmann modeling of binary flow based on the conservative Allen–Cahn equation” Phys. Rev. E. 94, (2016). Copyright 2016 APS Publishing. Reproduced with permission from Fakhari et al., “Improved locality of the phase-field lattice-Boltzmann model for immiscible fluids at high density ratios” Phys. Rev. E. 96, (2017). Copyright 2017 APS Publishing.

central moments. The latter enforces the locality of the algorithm, thus reducing the involved run time. However, this tends to slightly deteriorate the accuracy of the method. Given all these observations, we can conclude that the proposed approach represents a potential candidate to perform reliable computations of multiphase and multicomponent flows.

SUPPLEMENTARY MATERIAL

See the [supplementary material](#) for the script D3Q19-CentralMoments-PhaseField.m, which allows the reader to perform all the symbolic manipulations to derive the models presented in this paper. The sample C++ program Zalesak.cpp allows the reader to reproduce the results of the Zalesak disk case.

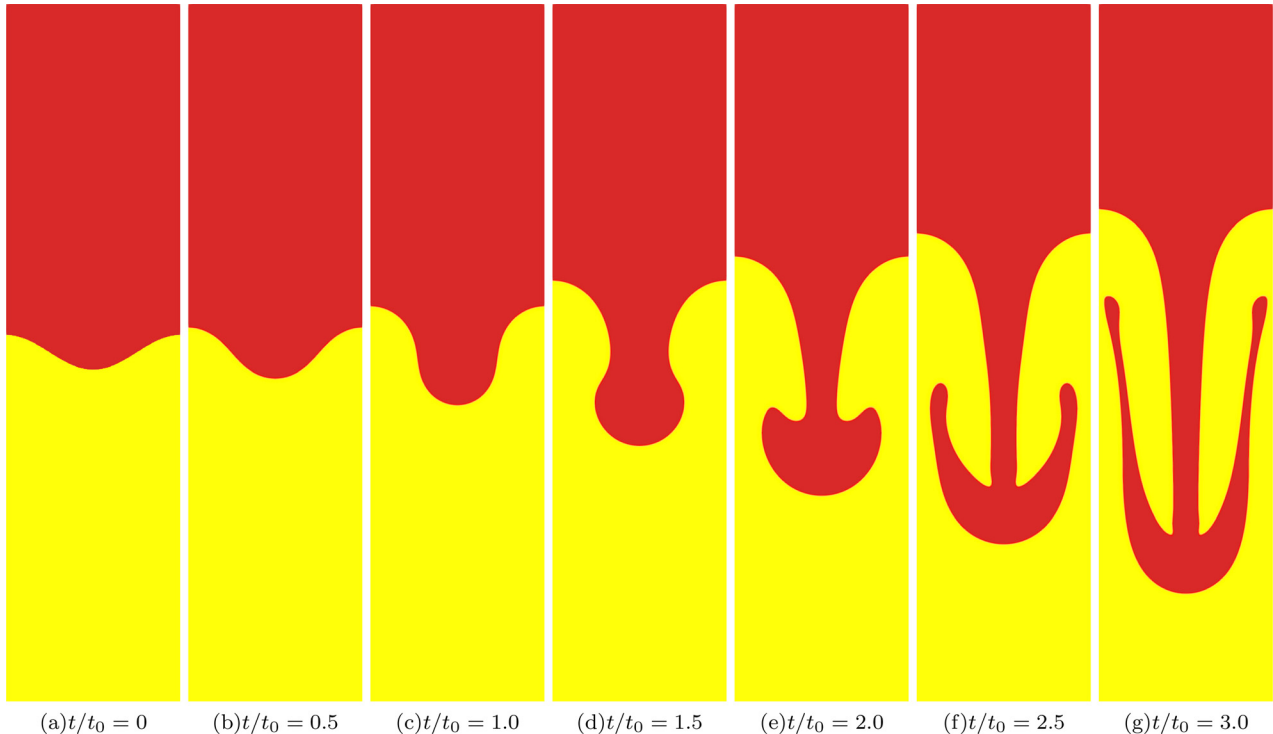


FIG. 12. Two-dimensional Rayleigh–Taylor instability at $Re = 256$: evolution of the interface at (a) $t/t_0 = 0$, (b) $t/t_0 = 0.5$, (c) $t/t_0 = 1.0$, (d) $t/t_0 = 1.5$, (e) $t/t_0 = 2.0$, (f) $t/t_0 = 2.5$ and (g) $t/t_0 = 3.0$. Red and yellow colors correspond to heavy and light fluids, respectively.

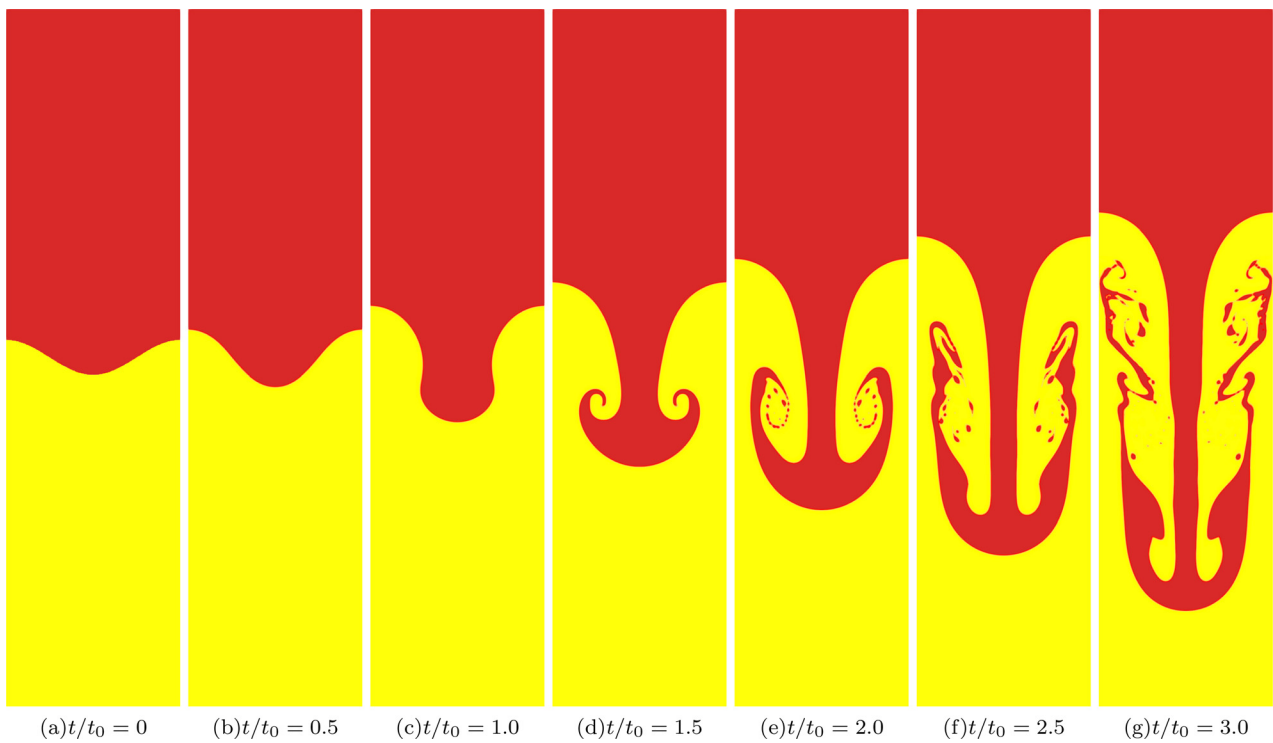


FIG. 13. Two-dimensional Rayleigh-Taylor instability at $Re = 3000$: evolution of the interface at (a) $t/t_0 = 0$, (b) $t/t_0 = 0.5$, (c) $t/t_0 = 1.0$, (d) $t/t_0 = 1.5$, (e) $t/t_0 = 2.0$, (f) $t/t_0 = 2.5$ and (g) $t/t_0 = 3.0$. Red and yellow colors correspond to heavy and light fluids, respectively.

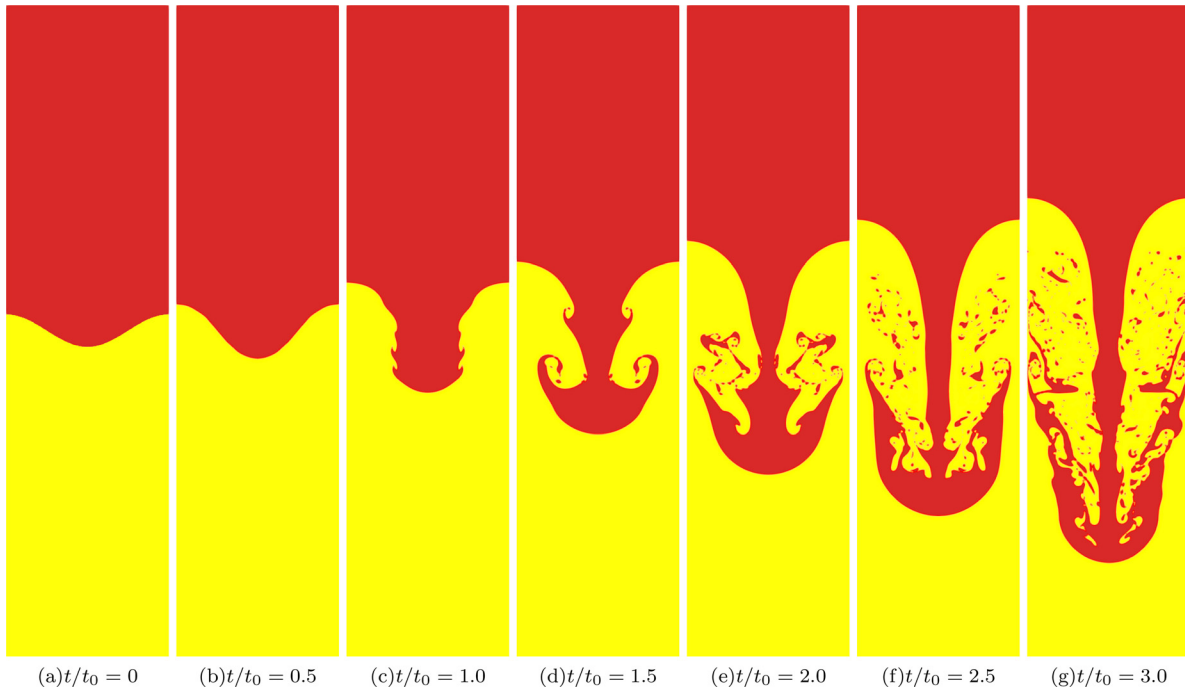


FIG. 14. Two-dimensional Rayleigh-Taylor instability at $Re = 30000$: evolution of the interface at (a) $t/t_0 = 0$, (b) $t/t_0 = 0.5$, (c) $t/t_0 = 1.0$, (d) $t/t_0 = 1.5$, (e) $t/t_0 = 2.0$, (f) $t/t_0 = 2.5$ and (g) $t/t_0 = 3.0$. Red and yellow colors correspond to heavy and light fluids, respectively.

TABLE VIII. Two-dimensional Rayleigh–Taylor instability at $\text{Re} = 30\,000$: vertical position of the spike of the interface normalized by the width of the domain at representative time instants.

t/t_0	0	0.5	1.0	1.5	2	2.5	3.0
y^\dagger	1.900	1.829	1.620	1.365	1.118	0.863	0.575

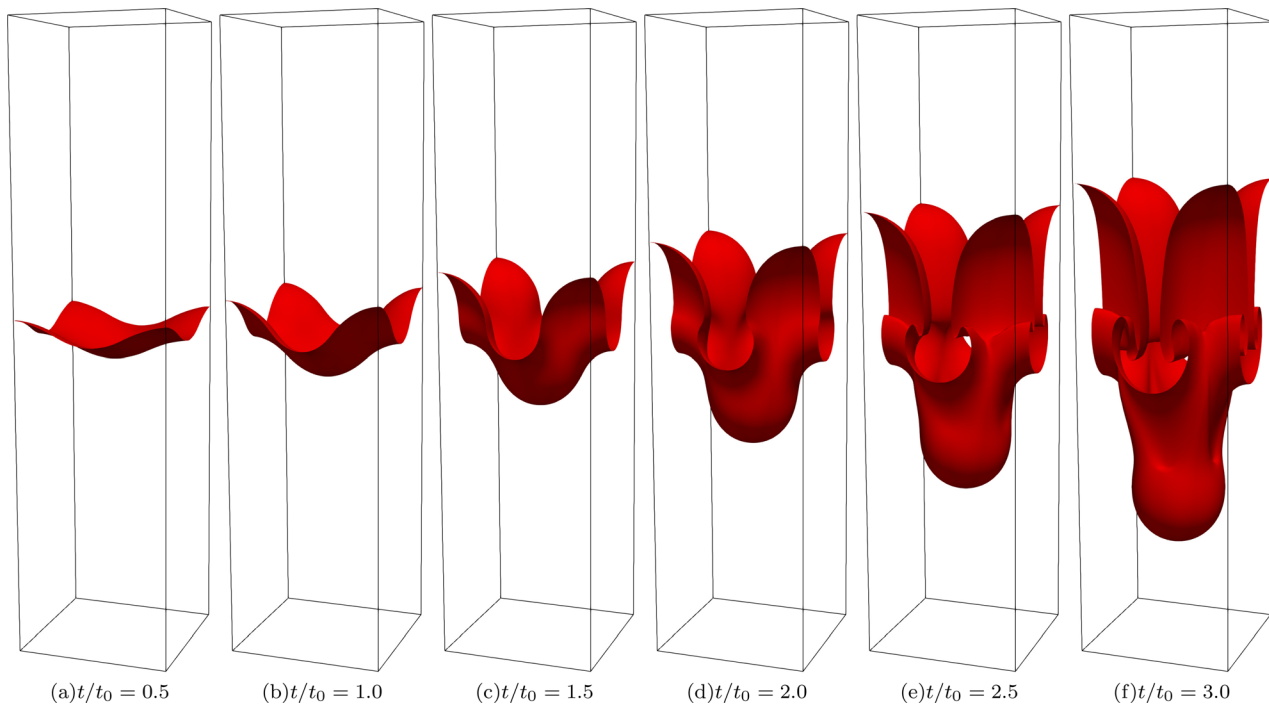


FIG. 15. Three-dimensional Rayleigh–Taylor instability: evolution of the interface at (a) $t/t_0 = 0.5$, (b) $t/t_0 = 1.0$, (c) $t/t_0 = 1.5$, (d) $t/t_0 = 2.0$, (e) $t/t_0 = 2.5$ and (f) $t/t_0 = 3.0$ when $\text{Re} = 256$.

TABLE IX. Rayleigh–Taylor instability: time evolution of the position of the spike of the interface at salient time instants. Present results are compared to those from (i) present scheme with finite differences (FD), (ii) present scheme with moments (Mom), (iii) the D3Q19-CGM-CM-LBM [74] (iv) the D3Q27-CGM-CM-LBM,⁶² (v) a D3Q27-CGM-MRT LB study based on the color-gradient method.²⁸ Reproduced with permission from Saito *et al.*, “Lattice Boltzmann modeling and simulation of liquid jet breakup,” *Phys. Rev. E* **96**, 013317 (2017). Copyright 2017 Authors, licensed under a Creative Commons Attribution (CC BY) License, (vi) a D3Q15-BGK LB model for multiphase flows,⁹⁴ (vii) a D3Q19-phase-field-MRT LB scheme,⁹⁵ and (viii) a solution of the coupled Navier–Stokes–Cahn–Hilliard equations.⁹⁶ Reproduced with permission from De Rosis and Coreixas, “Multiphysics flow simulations using D3Q19 lattice Boltzmann methods based on central moments,” *Phys. Fluids* **32**, 117101 (2020). Copyright 2020 AIP Publishing. Reproduced with permission from De Rosis *et al.*, “Universal formulation of central-moments-based lattice Boltzmann method with external forcing for the simulation of multiphysics phenomena,” *Phys. Fluids* **31**, 117102 (2019). Copyright 2019 AIP Publishing. Reproduced with permission from He *et al.*, “On the three-dimensional Rayleigh–Taylor instability,” *Phys. Fluids* **11**, 1 (1999). Copyright 1999 AIP Publishing. Reproduced with permission from Wang *et al.*, “Three-dimensional phase-field lattice Boltzmann model for incompressible multiphase flows,” *J. Comput. Sci.* **17**, 340–356 (2016). Copyright 2016 Elsevier. Reproduced with permission from Lee and Kim, “Numerical simulation of the three-dimensional Rayleigh–Taylor instability,” *Comput. Math. Appl. Comput. Sci.* **66**, 1466–1474 (2013). Copyright 2013 Elsevier.

t/t_0	FD	Mom	Ref. 74	Ref. 62	Ref. 28	Ref. 94	Ref. 95	Ref. 96
0.0	1.898	1.898	1.897	1.897	1.895	1.887	1.888	1.904
0.5	1.858	1.850	1.897	1.897	1.864	1.839	1.860	1.869
1.0	1.741	1.711	1.753	1.753	1.763	1.744	1.755	1.776
1.5	1.553	1.504	1.592	1.591	1.587	1.555	1.569	1.618
2.0	1.304	1.256	1.381	1.378	1.357	1.312	1.325	1.396
2.5	1.001	0.988	1.126	1.121	1.085	1.022	1.037	1.149
3.0	0.648	0.711	0.844	0.791	0.788	0.712	0.740	0.863

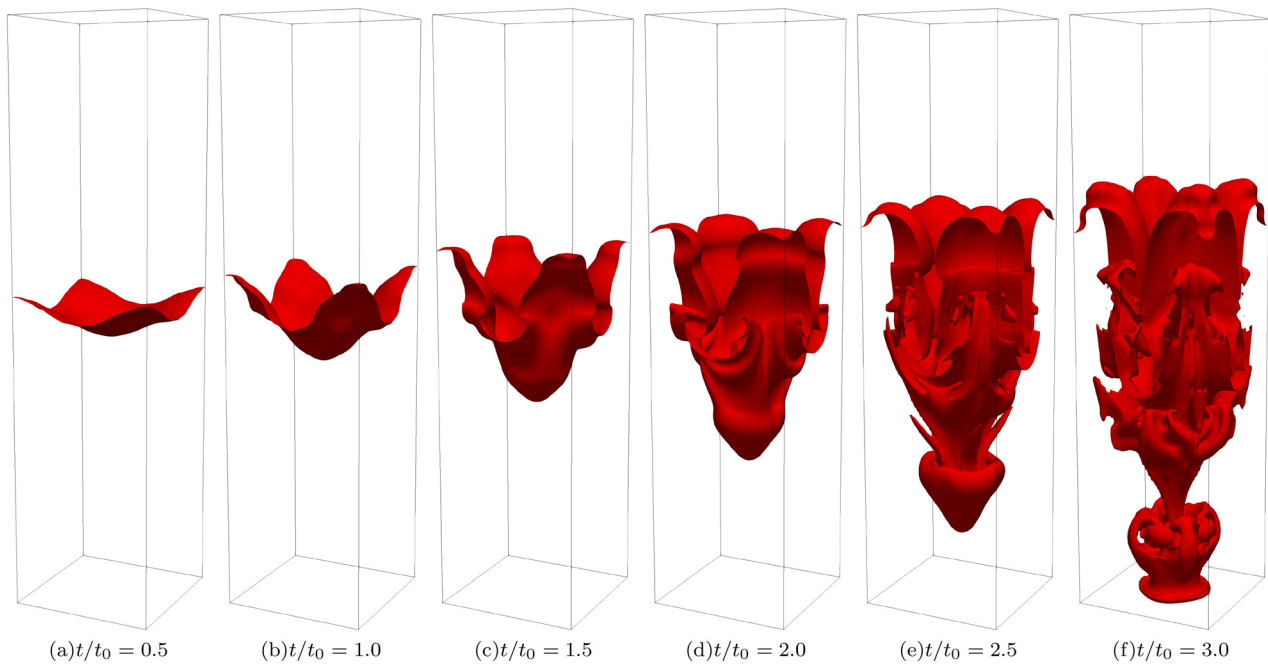


FIG. 16. Three-dimensional Rayleigh–Taylor instability: evolution of the interface at (a) $t/t_0 = 0.5$, (b) $t/t_0 = 1.0$, (c) $t/t_0 = 1.5$, (d) $t/t_0 = 2.0$, (e) $t/t_0 = 2.5$ and (f) $t/t_0 = 3.0$ when $\text{Re} = 3000$.

TABLE X. Three-dimensional Rayleigh–Taylor instability at $\text{Re} = 30\,000$: vertical position of the spike of the interface normalized by the width of the domain at representative time instants.

t/t_0	0	0.5	1.0	1.5	2	2.5	3.0
y^\dagger	1.898	1.848	1.680	1.384	0.964	0.436	0

APPENDIX: ALGORITHM OF COMPUTATION

Within the typical time step, the proposed scheme performs the following actions:

- (1) Compute the macroscopic variables

$$\begin{aligned}\tilde{p} &= \sum_i f_i, \\ \mathbf{u} &= \sum_i f_i \mathbf{c}_i + \frac{\mathbf{F}}{2\rho}, \\ \phi &= \sum_i g_i.\end{aligned}\quad (\text{A1})$$

- (2) Evaluate the spatial derivatives of the order parameter, velocity and density

$$\begin{aligned}\nabla\phi &= \frac{1}{c_s^2} \sum_i w_i \mathbf{c}_i \phi (\mathbf{x} + \mathbf{c}_i), \\ \nabla\mathbf{u} &= \frac{1}{c_s^2} \sum_i w_i \mathbf{c}_i \mathbf{u} (\mathbf{x} + \mathbf{c}_i), \\ \nabla\rho &= \frac{\rho_H - \rho_L}{\phi_H - \phi_L} \nabla\phi.\end{aligned}\quad (\text{A2})$$

Alternatively, $\nabla\phi$ can be computed directly from the first-order central moments as

$$\begin{aligned}\nabla_x\phi &= -k_{1,\phi}, \\ \nabla_y\phi &= -k_{2,\phi}, \\ \nabla_z\phi &= -k_{3,\phi}.\end{aligned}\quad (\text{A3})$$

- (3) Interpolate the relaxation time τ

$$\tau = \tau_L + \frac{\phi - \phi_L}{\phi_H - \phi_L} (\tau_H - \tau_L) \quad (\text{A4})$$

and get the kinematic viscosity $\nu = \tau c_s^2$.

- (4) Obtain the forces $\mathbf{F} = \mathbf{F}_s + \mathbf{F}_p + \mathbf{F}_\nu + \mathbf{F}_b$

$$\begin{aligned}\mathbf{F}_s &= \mu_\phi \nabla\phi \\ \mathbf{F}_p &= -\tilde{p} c_s^2 \nabla\rho, \\ \mathbf{F}_\nu &= \nu [\nabla\mathbf{u} + (\nabla\mathbf{u})^\top] \cdot \nabla\rho.\end{aligned}\quad (\text{A5})$$

\mathbf{F}_b accounts for any external body forces (e.g., gravity).

- (5) Correct the fluid velocity

$$\mathbf{u} = \sum_i f_i \mathbf{c}_i + \frac{\mathbf{F}}{2\rho}. \quad (\text{A6})$$

- (6) Determine the vector \mathbf{F}_ϕ

$$\mathbf{F}_\phi = c_s^2 \frac{1 - 4(\phi - \phi_0)^2}{\xi} \cdot \frac{\nabla\phi}{|\nabla\phi|}. \quad (\text{A7})$$

- (7) Compute the only non-zero pre-collision central moments

$$\begin{aligned}
k_5 &= f_1 + f_2 - f_3 - f_4 + f_{11} + f_{12} + f_{13} \\
&\quad + f_{14} - f_{15} - f_{16} - f_{17} - f_{18} + (u_x^2 - u_y^2)(\tilde{p} - 2), \\
k_6 &= f_3 + f_4 - f_5 - f_6 + f_7 + f_8 + f_9 \\
&\quad + f_{10} - f_{11} - f_{12} - f_{13} - f_{14} + (u_y^2 - u_z^2)(\tilde{p} - 2), \\
k_7 &= f_7 + f_8 - f_9 - f_{10} + u_x u_y (\tilde{p} - 2), \\
k_8 &= f_{11} + f_{12} - f_{13} - f_{14}, + u_x u_z (\tilde{p} - 2), \\
k_9 &= f_{15} + f_{16} - f_{17} - f_{18} + u_y u_z (\tilde{p} - 2), \\
k_{1,\phi} &= g_1 - g_2 + g_7 - g_8 + g_9 - g_{10} + g_{11} - g_{12} + g_{13} - g_{14} - \phi u_x, \\
k_{2,\phi} &= g_3 - g_4 + g_7 - g_8 - g_9 + g_{10} + g_{15} - g_{16} + g_{17} - g_{18} - \phi u_y, \\
k_{3,\phi} &= g_5 - g_6 + g_{11} - g_{12} - g_{13} + g_{14} + g_{15} - g_{16} - g_{17} + g_{18} - \phi u_z. \\
\end{aligned} \tag{A8}$$

(8) Calculate the post-collision central moments $|k_i^*\rangle$

$$\begin{aligned}
k_0^* &= \tilde{p}, \\
k_1^* &= \frac{F_x}{2} - u_x(\tilde{p} - 1), \\
k_2^* &= \frac{F_y}{2} - u_y(\tilde{p} - 1), \\
k_3^* &= \frac{F_z}{2} - u_z(\tilde{p} - 1), \\
k_4^* &= \tilde{p} \left(1 + u_x^2 + u_y^2 + u_z^2 \right) - u_x^2 - u_y^2 - u_z^2, \\
k_5^* &= (1 - \omega)k_5 + (u_x^2 - u_y^2)(\tilde{p} - 1), \\
k_6^* &= (1 - \omega)k_6 + (u_y^2 - u_z^2)(\tilde{p} - 1), \\
k_7^* &= (1 - \omega)k_7 + u_x u_y (\tilde{p} - 1), \\
k_8^* &= (1 - \omega)k_8 + u_x u_z (\tilde{p} - 1), \\
k_9^* &= (1 - \omega)k_9 + u_y u_z (\tilde{p} - 1), \\
k_{10}^* &= \frac{F_y c_s^2}{2} - u_y (3u_x^2 + 1)(\tilde{p} - 1)c_s^2, \\
k_{11}^* &= \frac{F_x c_s^2}{2} - u_x (3u_y^2 + 1)(\tilde{p} - 1)c_s^2, \\
k_{12}^* &= \frac{F_z c_s^2}{2} - u_z (3u_x^2 + 1)(\tilde{p} - 1)c_s^2, \\
k_{13}^* &= \frac{F_x c_s^2}{2} - u_x (3u_z^2 + 1)(\tilde{p} - 1)c_s^2, \\
k_{14}^* &= \frac{F_y c_s^2}{2} - u_z (3u_y^2 + 1)(\tilde{p} - 1)c_s^2, \\
k_{15}^* &= \frac{F_z c_s^2}{2} - u_y (3u_z^2 + 1)(\tilde{p} - 1)c_s^2, \\
k_{16}^* &= \tilde{p} \left[c_s^4 + c_s^2 \left(u_x^2 + u_y^2 \right) + u_x^2 u_y^2 \right] - c_s^2 \left(u_x^2 + u_y^2 \right) - u_x^2 u_y^2, \\
k_{17}^* &= \tilde{p} \left[c_s^4 + c_s^2 \left(u_x^2 + u_z^2 \right) + u_x^2 u_z^2 \right] - c_s^2 \left(u_x^2 + u_z^2 \right) - u_x^2 u_z^2, \\
k_{18}^* &= \tilde{p} \left[c_s^4 + c_s^2 \left(u_y^2 + u_z^2 \right) + u_y^2 u_z^2 \right] - c_s^2 \left(u_y^2 + u_z^2 \right) - u_y^2 u_z^2
\end{aligned} \tag{A9}$$

and $|k_{i,\phi}^*\rangle$

$$\begin{aligned}
k_{0,\phi}^* &= \phi, \\
k_{1,\phi}^* &= (1 - \omega_\phi)k_{1,\phi} + (1 - \omega_\phi/2)F_{x,\phi}, \\
k_{2,\phi}^* &= (1 - \omega_\phi)k_{2,\phi} + (1 - \omega_\phi/2)F_{y,\phi}, \\
k_{3,\phi}^* &= (1 - \omega_\phi)k_{3,\phi} + (1 - \omega_\phi/2)F_{z,\phi}, \\
k_{4,\phi}^* &= \phi, \\
k_{10,\phi}^* &= F_{y,\phi} c_s^2 / 2, \\
k_{11,\phi}^* &= F_{x,\phi} c_s^2 / 2, \\
k_{12,\phi}^* &= F_{z,\phi} c_s^2 / 2, \\
k_{13,\phi}^* &= F_{x,\phi} c_s^2 / 2, \\
k_{14,\phi}^* &= F_{z,\phi} c_s^2 / 2, \\
k_{15,\phi}^* &= F_{y,\phi} c_s^2 / 2, \\
k_{16,\phi}^* &= \phi c_s^4, \\
k_{17,\phi}^* &= \phi c_s^4, \\
k_{18,\phi}^* &= \phi c_s^4.
\end{aligned} \tag{A10}$$

(9) Reconstruct post-collision populations for the flow and phase fields by the two-steps strategy

$$\begin{aligned}
|f_i^*\rangle &= \mathbf{M}^{-1} \mathbf{N}^{-1} |k_i^*\rangle, \\
|g_i^*\rangle &= \mathbf{M}^{-1} \mathbf{N}^{-1} |g_{i,\phi}^*\rangle.
\end{aligned} \tag{A11}$$

(10) Advance in time by streaming both the sets of populations as

$$\begin{aligned}
|f_i(\mathbf{x} + \mathbf{c}_i, t + 1)\rangle &= |f_i^*(\mathbf{x}, t)\rangle, \\
|g_i(\mathbf{x} + \mathbf{c}_i, t + 1)\rangle &= |g_i^*(\mathbf{x}, t)\rangle.
\end{aligned} \tag{A12}$$

DATA AVAILABILITY

The data that support the findings of this study are available within the article.

REFERENCES

- ¹D. M. Anderson, G. B. McFadden, and A. A. Wheeler, "Diffuse-interface methods in fluid mechanics," *Annu. Rev. Fluid Mech.* **30**, 139–165 (1998).
- ²J. W. Cahn and J. E. Hilliard, "Free energy of a nonuniform system. I. Interfacial free energy," *J. Chem. Phys.* **28**, 258–267 (1958).
- ³S. M. Allen and J. W. Cahn, "Mechanisms of phase transformations within the miscibility gap of fe-rich fe-al alloys," *Acta Metall.* **24**, 425–437 (1976).
- ⁴D. Jacqmin, "Calculation of two-phase Navier-Stokes flows using phase-field modeling," *J. Comput. Phys.* **155**, 96–127 (1999).
- ⁵V. E. Badalassi, H. D. Ceniceros, and S. Banerjee, "Computation of multiphase systems with phase field models," *J. Comput. Phys.* **190**, 371–397 (2003).
- ⁶A. Belhocine, "Numerical study of heat transfer in fully developed laminar flow inside a circular tube," *Int. J. Adv. Manuf. Technol.* **85**, 2681–2692 (2016).
- ⁷A. Belhocine and W. Z. Wan Omar, "An analytical method for solving exact solutions of the convective heat transfer in fully developed laminar flow through a circular tube," *Heat Transfer Asian Res.* **46**, 1342–1353 (2017).
- ⁸A. Belhocine and O. I. Abdullah, "Numerical simulation of thermally developing turbulent flow through a cylindrical tube," *Int. J. Adv. Manuf. Technol.* **102**, 2001–2012 (2019).
- ⁹A. Belhocine and W. Z. W. Omar, "Analytical solution and numerical simulation of the generalized levèque equation to predict the thermal boundary layer," *Math. Comput. Simul.* **180**, 43–60 (2021).
- ¹⁰R. Benzi, S. Succi, and M. Vergassola, "The lattice Boltzmann equation: Theory and applications," *Phys. Rep.* **222**, 145–197 (1992).

- ¹¹T. Krüger, H. Kusumaatmaja, A. Kuzmin, O. Shardt, G. Silva, and E. M. Viggen, *The Lattice Boltzmann Method: Principles and Practice* (Springer International Publishing, 2017).
- ¹²S. Succi, *The Lattice Boltzmann Equation: For Complex States of Flowing Matter* (Oxford University Press, 2018).
- ¹³K. Kutscher, M. Geier, and M. Krafczyk, "Massively parallel lattice Boltzmann simulations of turbulent flow over and inside porous media," in *Fundamentals of High Lift for Future Civil Aircraft* (Springer, 2021), pp. 513–527.
- ¹⁴J. Chin, "Lattice Boltzmann simulation of the flow of binary immiscible fluids with different viscosities using the shan-chen microscopic interaction model," *Philos. Trans. R. Soc. London, Ser. A* **360**, 547–558 (2002).
- ¹⁵E. S. Boek and M. Venturoli, "Lattice-Boltzmann studies of fluid flow in porous media with realistic rock geometries," *Comput. Math. Appl.* **59**, 2305–2314 (2010).
- ¹⁶D. M. Holman, R. M. Brionnaud, and Z. Abiza, "Solution to industry benchmark problems with the lattice-Boltzmann code xflow," in Proceeding in the European Congress on Computational Methods in Applied Sciences and Engineering (ECCOMAS), 2012.
- ¹⁷E. Fares, "Unsteady flow simulation of the ahmed reference body using a lattice Boltzmann approach," *Comput. Fluids* **35**, 940–950 (2006).
- ¹⁸J. Latt, O. Malaspinas, D. Kontaxakis, A. Parmigiani, D. Lagrava, F. Brogi, M. B. Belgacem, Y. Thorimbert, S. Leclaire, S. Li *et al.*, "Palabos: Parallel lattice Boltzmann solver," *Comput. Math. Appl.* **81**, 334–350 (2021).
- ¹⁹Y. Feng, J. Miranda, S. Guo, J. Jacob, and P. Sagaut, "Prolb: A lattice Boltzmann solver of large-eddy simulation for atmospheric boundary layer flows," *J. Adv. Model. Earth Syst.* **13**, e2020MS002107 (2020).
- ²⁰D. Grunau, S. Chen, and K. Eggert, "A lattice Boltzmann model for multiphase fluid flows," *Phys. Fluids A* **5**, 2557–2562 (1993).
- ²¹L. Chen, Q. Kang, Y. Mu, Y.-L. He, and W.-Q. Tao, "A critical review of the pseudopotential multiphase lattice Boltzmann model: Methods and applications," *Int. J. Heat Mass Transfer* **76**, 210–236 (2014).
- ²²H. Huang, M. Sukop, and X. Lu, *Multiphase Lattice Boltzmann Methods: Theory and Application* (John Wiley & Sons Inc, 2015).
- ²³A. K. Gunstensen and D. H. Rothman, "Microscopic modeling of immiscible fluids in three dimensions by a lattice Boltzmann method," *EPL* **18**, 157 (1992).
- ²⁴D. H. Rothman and J. M. Keller, "Immiscible cellular-automaton fluids," *J. Stat. Phys.* **52**, 1119–1127 (1988).
- ²⁵T. Reis and T. N. Phillips, "Lattice Boltzmann model for simulating immiscible two-phase flows," *J. Phys. A: Math. Theor.* **40**, 4033–4053 (2007).
- ²⁶S. Leclaire, M. Reggio, and J.-Y. Trepanier, "Numerical evaluation of two recoloring operators for an immiscible two-phase flow lattice Boltzmann model," *Appl. Math. Modell.* **36**, 2237–2252 (2012).
- ²⁷M. Latva-Kokko and D. H. Rothman, "Diffusion properties of gradient-based lattice Boltzmann models of immiscible fluids," *Phys. Rev. E* **71**, 056702 (2005).
- ²⁸S. Saito, Y. Abe, and K. Koyama, "Lattice Boltzmann modeling and simulation of liquid jet breakup," *Phys. Rev. E* **96**, 013317 (2017).
- ²⁹S. Saito, A. De Rosis, A. Festuccia, A. Kaneko, Y. Abe, and K. Koyama, "Color-gradient lattice Boltzmann model with nonorthogonal central moments: Hydrodynamic melt-jet breakup simulations," *Phys. Rev. E* **98**, 013305 (2018).
- ³⁰S. Bakhsian, H. S. Rabbani, S. A. Hosseini, and N. Shokri, "New insights into complex interactions between heterogeneity and wettability influencing two-phase flow in porous media," *Geophys. Res. Lett.* **47**, e2020GL088187, <https://doi.org/10.1029/2020GL088187> (2020).
- ³¹S. Bakhsian, M. Murakami, S. A. Hosseini, and Q. Kang, "Scaling of imbibition front dynamics in heterogeneous porous media," *Geophys. Res. Lett.* **47**, e2020GL087914, <https://doi.org/10.1029/2020GL087914> (2020).
- ³²X. Shan and H. Chen, "Lattice Boltzmann model for simulating flows with multiple phases and components," *Phys. Rev. E* **47**, 1815 (1993).
- ³³M. Sbragaglia, R. Benzi, L. Biferale, S. Succi, K. Sugiyama, and F. Toschi, "Generalized lattice Boltzmann method with multirange pseudopotential," *Phys. Rev. E* **75**, 026702 (2007).
- ³⁴G. Falcucci, S. Ubertini, and S. Succi, "Lattice Boltzmann simulations of phase-separating flows at large density ratios: The case of doubly-attractive pseudopotentials," *Soft Matter* **6**, 4357–4365 (2010).
- ³⁵R. Huang, H. Wu, and N. A. Adams, "Eliminating cubic terms in the pseudopotential lattice Boltzmann model for multiphase flow," *Phys. Rev. E* **97**, 053308 (2018).
- ³⁶M. R. Swift, E. Orlandini, W. Osborn, and J. Yeomans, "Lattice Boltzmann simulations of liquid-gas and binary fluid systems," *Phys. Rev. E* **54**, 5041 (1996).
- ³⁷T. Inamuro, N. Konishi, and F. Ogino, "A galilean invariant model of the lattice Boltzmann method for multiphase fluid flows using free-energy approach," *Comput. Phys. Commun.* **129**, 32–45 (2000).
- ³⁸C. Pooley and K. Furtado, "Eliminating spurious velocities in the free-energy lattice Boltzmann method," *Phys. Rev. E* **77**, 046702 (2008).
- ³⁹H. Liu, A. J. Valocchi, Y. Zhang, and Q. Kang, "Lattice Boltzmann phase-field modeling of thermocapillary flows in a confined microchannel," *J. Comput. Phys.* **256**, 334–356 (2014).
- ⁴⁰H. Liang, B. Shi, Z. Guo, and Z. Chai, "Phase-field-based multiple-relaxation-time lattice Boltzmann model for incompressible multiphase flows," *Phys. Rev. E* **89**, 053320 (2014).
- ⁴¹M. Geier, A. Fakhari, and T. Lee, "Conservative phase-field lattice Boltzmann model for interface tracking equation," *Phys. Rev. E* **91**, 063309 (2015).
- ⁴²A. Fakhari, T. Mitchell, C. Leonardi, and D. Bolster, "Improved locality of the phase-field lattice-Boltzmann model for immiscible fluids at high density ratios," *Phys. Rev. E* **96**, 053301 (2017).
- ⁴³A. Fakhari, M. Geier, and D. Bolster, "A simple phase-field model for interface tracking in three dimensions," *Comput. Math. Appl.* **78**, 1154–1165 (2019).
- ⁴⁴H. Wang, X. Yuan, H. Liang, Z. Chai, and B. Shi, "A brief review of the phase-field-based lattice Boltzmann method for multiphase flows," *Capillarity* **2**, 33–52 (2019).
- ⁴⁵Y. Zu and S. He, "Phase-field-based lattice Boltzmann model for incompressible binary fluid systems with density and viscosity contrasts," *Phys. Rev. E* **87**, 043301 (2013).
- ⁴⁶H. Zheng, C. Shu, and Y. Chew, "Lattice Boltzmann interface capturing method for incompressible flows," *Phys. Rev. E* **72**, 056705 (2005).
- ⁴⁷H. Liang, B. Shi, and Z. Chai, "Lattice Boltzmann modeling of three-phase incompressible flows," *Phys. Rev. E* **93**, 013308 (2016).
- ⁴⁸H. Wang, Z. Chai, B. Shi, and H. Liang, "Comparative study of the lattice Boltzmann models for Allen-Cahn and Cahn-Hilliard equations," *Phys. Rev. E* **94**, 033304 (2016).
- ⁴⁹H. Liang, J. Xu, J. Chen, H. Wang, Z. Chai, and B. Shi, "Phase-field-based lattice Boltzmann modeling of large-density-ratio two-phase flows," *Phys. Rev. E* **97**, 033309 (2018).
- ⁵⁰F. Ren, B. Song, M. C. Sukop, and H. Hu, "Improved lattice Boltzmann modeling of binary flow based on the conservative Allen-Cahn equation," *Phys. Rev. E* **94**, 023311 (2016).
- ⁵¹A. Begmohammadi, R. Haghani-Hassan-Abadi, A. Fakhari, and D. Bolster, "Study of phase-field lattice Boltzmann models based on the conservative allen-cahn equation," *Phys. Rev. E* **102**, 023305 (2020).
- ⁵²Y. Zu, A. Li, and H. Wei, "Phase-field lattice Boltzmann model for interface tracking of a binary fluid system based on the allen-cahn equation," *Phys. Rev. E* **102**, 053307 (2020).
- ⁵³G. Gruszczyński, T. Mitchell, C. Leonardi, T. Barber *et al.*, "A cascaded phase-field lattice Boltzmann model for the simulation of incompressible, immiscible fluids with high density contrast," *Comput. Math. Appl.* **79**, 1049–1071 (2020).
- ⁵⁴M. Geier, A. Greiner, and J. Korvink, "Cascaded digital lattice Boltzmann automata for high Reynolds number flow," *Phys. Rev. E* **73**, 066705 (2006).
- ⁵⁵S. A. Hosseini, H. Safari, and D. Thevenin, "Lattice Boltzmann solver for multiphase flows: Application to high weber and Reynolds numbers," *Entropy* **23**, 166 (2021).
- ⁵⁶O. Malaspinas, "Increasing stability and accuracy of the lattice Boltzmann scheme: Recursivity and regularization," preprint [arXiv:1505.06900](https://arxiv.org/abs/1505.06900) (2015).
- ⁵⁷C. Coreixas, G. Wissocq, G. Puigt, J.-F. Boussuge, and P. Sagaut, "Recursive regularization step for high-order lattice Boltzmann methods," *Phys. Rev. E* **96**, 033306 (2017).
- ⁵⁸A. De Rosis and K. H. Luo, "Role of higher-order hermite polynomials in the central-moments-based lattice Boltzmann framework," *Phys. Rev. E* **99**, 013301 (2019).
- ⁵⁹A. De Rosis, "A central moments-based lattice Boltzmann scheme for shallow water equations," *Comput. Methods Appl. Mech. Eng.* **319**, 379–392 (2017).
- ⁶⁰A. De Rosis, "Preconditioned lattice Boltzmann method for steady flows: A noncascaded central-moments-based approach," *Phys. Rev. E* **96**, 063308 (2017).
- ⁶¹A. De Rosis, E. Lévéque, and R. Chahine, "Advanced lattice Boltzmann scheme for high-Reynolds-number magneto-hydrodynamic flows," *J. Turbul.* **19**, 446–462 (2018).

- ⁶²A. De Rosis, R. Huang, and C. Coreixas, “Universal formulation of central-moments-based lattice Boltzmann method with external forcing for the simulation of multiphysics phenomena,” *Phys. Fluids* **31**, 117102 (2019).
- ⁶³M. B. Asadi, A. De Rosis, and S. Zendehboudi, “Central-moments-based lattice Boltzmann for associating fluids: A new integrated approach,” *J. Phys. Chem. B* **124**, 2900–2913 (2020).
- ⁶⁴A. De Rosis and A. Tafuni, “A phase-field lattice Boltzmann method for the solution of water-entry and water-exit problems,” *Comput.-Aided Civ. Infrastruct. Eng.* (published online 2020).
- ⁶⁵E. Dinesh Kumar, S. Sannasiraj, and V. Sundar, “Phase field lattice Boltzmann model for air-water two phase flows,” *Phys. Fluids* **31**, 072103 (2019).
- ⁶⁶T. Mitchell, C. Leonardi, and A. Fakhari, “Development of a three-dimensional phase-field lattice Boltzmann method for the study of immiscible fluids at high density ratios,” *Int. J. Multiphase Flow* **107**, 1–15 (2018).
- ⁶⁷J. H. Ferziger, M. Perić, and R. L. Street, *Computational Methods for Fluid Dynamics* (Springer, 2002), Vol. 3.
- ⁶⁸P.-H. Chiu and Y.-T. Lin, “A conservative phase field method for solving incompressible two-phase flows,” *J. Comput. Phys.* **230**, 185–204 (2011).
- ⁶⁹P. Bhatnagar, E. Gross, and M. Krook, “A model for collision processes in gases. I. Small amplitude processes in charged and neutral one-component systems,” *Phys. Rev.* **94**, 511 (1954).
- ⁷⁰X. Shan, “Analysis and reduction of the spurious current in a class of multiphase lattice Boltzmann models,” *Phys. Rev. E* **73**, 047701 (2006).
- ⁷¹R. Adhikari and S. Succi, “Duality in matrix lattice Boltzmann models,” *Phys. Rev. E* **78**, 066701 (2008).
- ⁷²C. Coreixas, B. Chopard, and J. Latt, “Comprehensive comparison of collision models in the lattice Boltzmann framework: Theoretical investigations,” *Phys. Rev. E* **100**, 033305 (2019).
- ⁷³C. Coreixas, G. Wissocq, B. Chopard, and J. Latt, “Impact of collision models on the physical properties and the stability of lattice Boltzmann methods,” *Philos. Trans. R. Soc. A* **378**, 20190397 (2020).
- ⁷⁴A. De Rosis and C. Coreixas, “Multiphysics flow simulations using d3q19 lattice Boltzmann methods based on central moments,” *Phys. Fluids* **32**, 117101 (2020).
- ⁷⁵I. Karlin and P. Asinari, “Factorization symmetry in the lattice Boltzmann method,” *Physica A* **389**, 1530–1548 (2010).
- ⁷⁶M. E. McCracken and J. Abraham, “Multiple-relaxation-time lattice-Boltzmann model for multiphase flow,” *Phys. Rev. E* **71**, 036701 (2005).
- ⁷⁷L. Fei and K. H. Luo, “Consistent forcing scheme in the cascaded lattice Boltzmann method,” *Phys. Rev. E* **96**, 053307 (2017).
- ⁷⁸Z. Guo, C. Zheng, and B. Shi, “Discrete lattice effects on the forcing term in the lattice Boltzmann method,” *Phys. Rev. E* **65**, 046308 (2002).
- ⁷⁹L. Fei, K. H. Luo, and Q. Li, “Three-dimensional cascaded lattice Boltzmann method: Improved implementation and consistent forcing scheme,” *Phys. Rev. E* **97**, 053309 (2018).
- ⁸⁰P. Asinari, “Generalized local equilibrium in the cascaded lattice Boltzmann method,” *Phys. Rev. E* **78**, 016701 (2008).
- ⁸¹S. T. Zalesak, “Fully multidimensional flux-corrected transport algorithms for fluids,” *J. Comput. Phys.* **31**, 335–362 (1979).
- ⁸²M. Rudman, “Volume-tracking methods for interfacial flow calculations,” *Int. J. Numer. Methods Fluids* **24**, 671–691 (1997).
- ⁸³W. J. Rider and D. B. Kothe, “Reconstructing volume tracking,” *J. Comput. Phys.* **141**, 112–152 (1998).
- ⁸⁴E. Fadlun, R. Verzicco, P. Orlandi, and J. Mohd-Yusof, “Combined immersed-boundary finite-difference methods for three-dimensional complex flow simulations,” *J. Comput. Phys.* **161**, 35–60 (2000).
- ⁸⁵C. Peskin, “The immersed boundary method,” *Acta Numer.* **11**, 479–517 (2002).
- ⁸⁶R. Mittal and G. Iaccarino, “Immersed boundary methods,” *Annu. Rev. Fluid Mech.* **37**, 239–261 (2005).
- ⁸⁷Z.-G. Feng and E. Michaelides, “Robust treatment of no-slip boundary condition and velocity updating for the lattice-Boltzmann simulation of particulate flows,” *Comput. Fluids* **38**, 370–381 (2009).
- ⁸⁸A. De Rosis, S. Ubertini, and F. Ubertini, “A comparison between the interpolated bounce-back scheme and the immersed boundary method to treat solid boundary conditions for laminar flows in the lattice Boltzmann framework,” *J. Sci. Comput.* **61**, 477–489 (2014).
- ⁸⁹H. Wagner, “Über stoß-und gleitvorgänge an der oberfläche von flüssigkeiten,” *ZAMM-J. Appl. Math. Mech./Z. Angew. Math. Mech.* **12**, 193–215 (1932).
- ⁹⁰A. De Rosis, G. Falcucci, M. Porfiri, F. Ubertini, and S. Ubertini, “Hydroelastic analysis of hull slamming coupling lattice Boltzmann and finite element methods,” *Comput. Struct.* **138**, 24–35 (2014).
- ⁹¹D. H. Sharp, “An overview of Rayleigh-Taylor instability,” *Elsevier* **12**, 3–18 (1984).
- ⁹²D. L. Youngs, “Numerical simulation of turbulent mixing by Rayleigh-Taylor instability,” *Physica D* **12**, 32–44 (1984).
- ⁹³X. He, S. Chen, and R. Zhang, “A lattice Boltzmann scheme for incompressible multiphase flow and its application in simulation of Rayleigh-Taylor instability,” *J. Comput. Phys.* **152**, 642–663 (1999).
- ⁹⁴X. He, R. Zhang, S. Chen, and G. D. Doolen, “On the three-dimensional Rayleigh-Taylor instability,” *Phys. Fluids* **11**, 1143–1152 (1999).
- ⁹⁵N. Wang, H. Liu, and C. Zhang, “Three-dimensional phase-field lattice Boltzmann model for incompressible multiphase flows,” *J. Comput. Sci.* **17**, 340–356 (2016), discrete simulation of fluid dynamics, 2015.
- ⁹⁶H. G. Lee and J. Kim, “Numerical simulation of the three-dimensional Rayleigh-Taylor instability,” *Comput. Math. Appl.* **66**, 1466–1474 (2013).